Università degli Studi di Padova

Dipartimento di Fisica e Astronomia Galileo Galilei

MSc programme in Physics of Data

Nguyen Xuan Tung

Neural connectivity: a parallel in vitro and in silico analysis

final dissertation

Supervisors:
External Prof. Stefano Vassanelli
Internal Dr. Michele Allegra

academic year 2022-2023

List of Figures

Contents

Abstract

In this thesis, we will analyze neuronal recordings obtained by multi-electrode arrays (MEAs) on in vitro neuronal cultures from prof. Vassanelli's laboratory, trying to estimate synaptic connectivity between the neurons. To this aim, we will adopt several time series analysis techniques, including transfer entropy and coincidence analysis. We will develop a simple in silico dynamical model of the biological neuronal network, building on the standard Izhikevich model and adding some realistic constraints on the network topology. The model will be use to simulate neuronal time series and validate the connectivity inference methods. The end goal of the project is being able to reliably estimate how synaptic connectivity spontaneously varies in time.

Chapter 1

Introduction

The brain is one of the most complex systems we have ever known in the universe. It contains approximately 10^{11} cells with 10^3 connections each. It possesses an astonishing potential for up to 10^{14} connections. In order to understand the brain, we need to carefully analyze its connections. To gain insights into this complexity, researchers have long recognized that the neuron, as the fundamental unit of brain communication, plays an important role. A Neuron is a cell, which plays a crucial role in propagating signals over large distances within the brain. Networks of neurons have an ability to reorganize their structure and modify their connections in response to environmental changes and learning. This process, termed plasticity, is the key to understanding how connections within the network form and evolve. While we have gained some insight into the general principles of plasticity, how the detailed mechanisms are still not well understood.

However, the horizon of our knowledge has expanded with the advent of cutting-edge technologies. Among these innovations, microelectrode arrays (MEAs) have emerged as powerful tools that offer unprecedented insights into the dynamics of neural networks. By harnessing the potential of MEAs, we can now track and record the evolution of these networks over time, painting a clearer picture of how the brain's intricate tapestry of connections unfolds. This capability not only deepens our understanding of the brain's functioning but also paves the way for new vistas in neuroscience and beyond.

A fundamental prerequisite to study brain plasticity is the ability to track the evolution in time of network connections and their strengths. The goal of our the-

sis is to assess a range of methodological approaches, namely Transfer Entropy Analysis, Coincidences Analysis, and Functional Connectivity Analysis, for the purpose of reconstructing neural connectivity. This reconstruction process will be facilitated through simulations that closely emulate the intricate structures and dynamics of actual biological networks, as they are observed through the MEAs. In order to achieve this, we will design and conduct extensive simulations that replicate the conditions and complexities in the real biological neural networks. These simulations will serve as invaluable testbeds for evaluating the efficacy and accuracy of the methodologies in detecting network connections, a crucial step toward understanding the architecture of the networks. Upon validating and refining these methodologies through our simulated experiments, the next crucial phase of our investigation requires the practical application to authentic neural recordings obtained via MEAs. This empirical extension represents a central bridge between theoretical exploration and real-world observations.

Chapter 2

Scientific background

2.1 Properties of cell membrane, membrane potential, ion channels

The cell membrane is the barrier between the cell and its environment and a gateway for communication and transport. It is constructed of lipids, proteins and carbohydrates. Membranes make it possible to form specialized compartments in eukaryotic cells. Transport processes involve exchange of ions, nutrients, metabolites and signaling molecules with the environment. The cell membrane can be modeled as a capacitor. The good insulator lipid bilayer separates two good conductors (solutions full of ions or electrolytes), so charge accumulates on its two sides and a voltage is measured between the two sides, called the membrane potential. The membrane potential (Em) is defined as the electric potential difference (voltage) which can be measured between the two sides of the membrane surrounding living cells: $E_m = j_i - j_e$ (internal (j_i) minus external (j_e) potential). The resting membrane potential of mammalian cells typically falls between -50 and -80 mV. The membrane potential is created by membrane transport mechanisms aided by ion channels, pumps, transporters, which move ions across the membrane. The action potential, or simply spike, is the best known cellular function associated with membrane potential changes. Spikes are primarily generated by nerve and muscle cells in response to appropriate stimuli and involve a change of the membrane potential in time, characteristic for the particular cell. Their duration ranges from a few ms to several hundred ms.

The membrane potential does not change if the net charge crossing the membrane, or net flux, is zero. There are two scenarios where this can happen. The first one is: for each individual ion the net flux is zero, that is, within unit time the same number of K+ ions leave passively as enter the cell, and the same is true for Na+ and other ions. This means a thermodynamic equilibrium, because there is no energy investment and the ion concentrations do not change in time. Since the electrochemical potential of each ion is equal on the two sides, each ion is in thermodynamic equilibrium. Such are the Nernst and Donnan equilibrium states [1]. The second is: the net flux is zero for all ions combined, but not for the individual ions. This situation can only be maintained by active transport mechanisms (pumps). In this case, at a given membrane potential only one ion species may be at equilibrium (but most often none of them are), and since the others are not at equilibrium, they are "trying" to cross the membrane, which can only be compensated by the ion pumps (otherwise the diffusion halts due to equilibration of concentration between two sides of the membrane). Cells can create electrical potential differences via diffusion potentials through ion selective pores such as ion channels (Goldman-Hodgkin-Katz equation).
The ion channels in the membrane can be represented by simple electrical circuit diagrams (Figure 1) [1]. In the circuit, we just add an extra battery representing the Nernst potential for the given ion, because there is a concentration gradient (and consequently potential difference) of the ion for which the ion channel is selective (Nernst potential, see below). Thus, we can consider that gradient as a battery with an electromotive force (emf) in series with the resistor. The modified current-voltage relationship then becomes:

$$I_X = G_X(E_M - E_X) \tag{1}$$

in which I_X is the current of a specific ion, G_X is the conductivity of the membrane for ion X, Em is the membrane potential and E_X is equilibrium potential of ion. The equilibrium or Nernst potential for ion (E_X) in general can be written as:

$$E_X = -\frac{RT}{zF} ln \frac{[X]_i}{[X]_o} \tag{2}$$

where R: the universal gas constant, T: absolute temperature, valency of ion X, F: Faraday constant, $[X]_i$ and $[X]_o$: intracellular and extracellular concentration ion X.

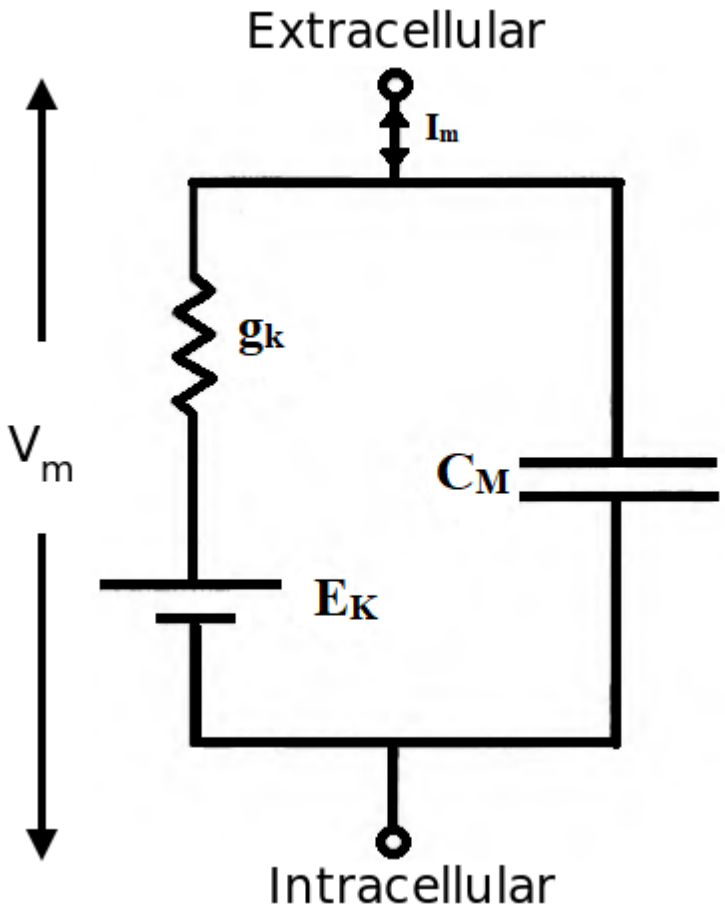

Figure 1: Electrical circuit diagram of potassium ion channel in membrane. V_m and I_m represents the voltage and current across the membrane, respectively. C_m represents the capacitance of the membrane. Where I_K, g_K, E_K show us the current, conductance, and the membrane potential for potassium (K) channel.

If an ion is permeating, then its electrochemical gradient (not its concentration gradient, since it has a charge) will determine which direction it will flow. In order to decide which direction a given ion will flow through an open ion channel, two values must be considered: the equilibrium (Nernst) potential calculated from the concentrations between the two sides of the membrane and the actual membrane potential of the cell. If the two values are equal, the ion is in equilibrium, the "driving force" is zero. The greater the difference between the membrane and the Nernst potential, the greater the driving force for the ion is.

2.2 Microelectrode arrays

Microelectrode array (MEA) systems are used for electrophysiological studies to characterize the behavior of neural networks [4]. They contain a grid of tightly spaced microscopic electrodes embedded in the bottom of each cell in a multi-cell system MEA plate. Culture cells are placed inside the plate, over the electrodes, to create a cohesive network. The function of electrical activity such as spike can be recorded extracellularly.

2.3 Izhikevich model

To model the neuron's activity, we need dynamical models. While some models (Hodgkin-Huxley) can give us extremely accurate simulation but are computationally expensive, others (integrate-and-fire neurons) are computationally effective but unrealistically simple, thus not able to reproduce rich spiking and bursting observed in real neurons. In this work we use a model that can take the best part of both models and combine them, called the Izhikevich model. In the Izhikevich model [12, 13], only four parameters need to be tuned, the complex behavior of cortical neurons is reproduced. The model can be represented in 2-D system of differential equations:

$$\frac{dv}{dt} = 0.04v^2 + 5v + 140 - u + I \tag{3}$$

$$\frac{du}{dt} = a(bv - u) \tag{4}$$

where v, u: dimensionless variables, a, b, c, d: dimensionless parameters, v: membrane potential, u: membrane recovery variable, which accounts for the activation of K+ ionic current and inactivation Na+ ionic current, I: synaptic currents or injected D/C current.
This causes the voltage inside the neuron to spike. But it also causes the K+ gates to open up, and K+ ions shoot out of the neuron which leads to the voltage drop right down. The voltage and K+ in this case are the membrane potential (v) and membrane recovery variable (u) respectively. The reset follows this formula:

$$\text{if } v \geq 30 \text{ mV, then } \begin{cases} v & \leftarrow & c \\ u & \leftarrow & u + d \end{cases} \tag{5}$$

the part $0.04v^2 + 5v + 140$ was obtained by fitting the spike initiation dynamics of real neurons, such that v is in mV and t is in ms. The resting potential is set between -70 mV and -60 mV. The threshold potential can be set between -55 mV and -40 mV.
We can make various choices of parameters a, b, c, d in order to reproduce various patterns of intrinsic firing. The relationship of parameters can be described as:

1. The parameter a describes the time scale of the recovery variable u. Smaller values result in slower recovery. A typical value is a= 0.02.

2. The parameter b describes the sensitivity of the recovery variable u to the subthreshold fluctuations of the membrane potential v. Greater values couple v and u more strongly resulting in possible subthreshold oscillations and low-threshold spiking dynamics. A typical value is b = 0.2.

3. The parameter c describes the after-spike reset value of the membrane potential v caused by the fast high-threshold K+ conductance. A typical value for c = -65 mV.

There are many different types of spiking and bursting inside a cell. All excitatory cells are categorized into following classes:

1. Regular spiking (RS) neurons: These are normal neurons. Prolonged stimuli cause the neurons to fire a few times in short periods, and the periods in-

crease. It has spike frequency adaptation.

2. Intrinsic bursting (IB) neurons: These neurons fire bursts of spikes followed by normal single spikes after.

3. Chattering (CH) neurons: These neurons fire closely spaced bursts of spikes.

All inhibitory cortical cells are divided in two following classes:

1. Fast spiking (FS) neurons: These neurons fire extremely quickly at high frequency without any adaptation.

2. Low-threshold spiking (LT) neurons: These neurons fire a high frequency train of spikes with noticeable spike frequency adaptation.

Chapter 3

Material and methods

3.1 Network of simulated neurons

Based on the Izhikevich model, we build a network model that reflects the real proportions of excitatory and inhibitory neurons found in the cortex. A network model with 80% excitatory neurons and 20% inhibitory neurons was designed with 80 excitatory neurons, each one randomly connected to 10 other neurons, which could be either excitatory or inhibitory [11]. The communication delay for each excitatory synapse was randomly chosen from a uniform distribution between 1 and 20 ms and remained constant over time. This delay allowed for realistic signal transmission within the network.

The 20 inhibitory neurons in the network were randomly connected to 10 excitatory post-synaptic neurons, forming 200 inhibitory synapses. The communication delay for these inhibitory synapses was fixed at 1 ms. Notably, we did not include inhibitory-to-inhibitory (I–I) connections in our network architecture. This omission led to the average firing rate of excitatory neurons ($5.12 \pm 0.08 Hz$) being lower than that of inhibitory neurons ($8.23 \pm 0.05 Hz$). Our simulations were conducted with 1-ms temporal precision and ran for up to 180 minutes.

In order to make the network dynamic, we introduced the dynamic change to the strength of excitatory synapses. During each simulation, the strength of excitatory synapses underwent dynamic changes based on a Hebbian exponential Spike-Timing Dependent Plasticity (STDP) rule.

When a presynaptic neuron i fired t ms before a post-synaptic neuron j, the synapse's strength from i to j (W_{ij}) was strengthened according to the formula

$\Delta W_{ij} = A_+ e^{-t/\tau}$ [8]. Conversely, when neuron j fired before neuron i, the synaptic strength W_{ij} was depressed as $W_{ij} = -A_- e^{(} - t/\tau)$. The decay time of the STDP rule was $\tau = 20ms$, with $A_+ = 0.1$ and $A_- = 0.12$.
To ensure the proper change in synapses, weights were updated by adding Wij to its previous value every 1 s. However, instead of resetting the weights to zero, we introduced a memory factor of 0.9 to retain a starting value for the subsequent update. This presence of the memory factor allowed the synaptic weights to evolve over a time-scale of a few minutes. To maintain network activity balance, the synaptic strengths were not allowed to exceed a cutoff value of 10 mV.

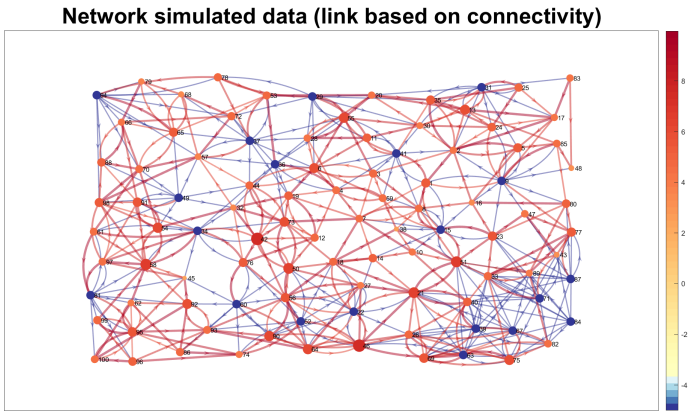

(A)

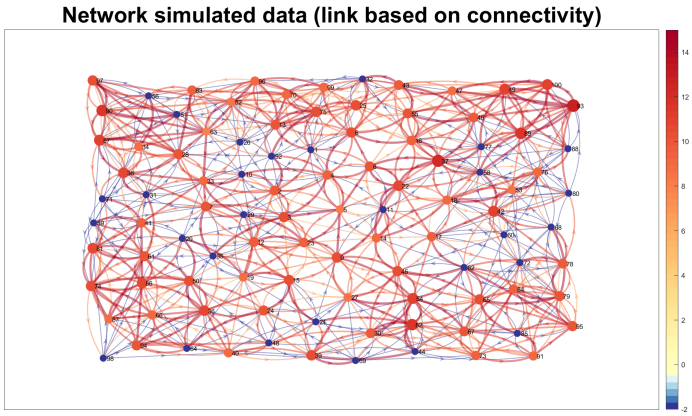

(B)

Figure 2: The network connectivity: (A) The network connectivity of simulated non bursty neurons. (B) The connectivity of simulated bursty neurons.

3.2 Network of real neurons

Wistar rats (Charles River) were maintained in the Animal Research Facility of the Department of Biomedical Sciences (University of Padua) under standard environmental conditions. All the procedures involving animals were realized according to Italian regulations for animal welfare (ethics approval from the Ital-

ian Ministry of Health, authorization number 522/2018-PR) and in compliance with the ARRIVE guidelines. Primary neurons were dissociated with papain from freshly dissected E18 rat embryos hippocampi as described previously [2]. About 310^4 neurons/cm^2 were plated on chips (pre-coated with $10\mu g/ml$ poly-L-lysine; Sigma-Aldrich), maintained in NeuroBasal™ Medium supplemented with 2% B-27 and transfected at DIV6. Culture media and transfection reagents, if not otherwise indicated, were purchased from Gibco™ (ThermoFisher Scientific).

3.3 Electrophysiology

CMOS-based HD-MEAs [3, 5] were used to record the extracellular signals of human iPSC-derived and rat primary neurons. The HD-MEA features 26 400 electrodes organized in a 120 × 220 grid within a total sensing area of 3.85 × 2.10 mm^2. The electrode area is 9.3 × 5.45 μm^2, and the center-to-center electrode distance (pitch) is 17.5 μm, which allows for recording of cell electrical activity at subcellular resolution. A user-selected configuration of 1024 electrodes can be simultaneously recorded from (see also the Experimental Section, HD-MEA Recordings). The HD-MEA features noise values of 2.4 $\mu Vrms$ in the action potential band of 0.3 – 10 kHz and has a programmable gain of up to 78 dB. The sampling frequency is 20 kHz. We used the MaxOne HD-MEA produced by MaxWell Biosystems AG (www.mxwbio.com) and the laboratory version of the same HD-MEA, [5] which only differs in the design of the printed circuit board (PCB).

3.4 Data analysis

3.4.1 Transfer entropy analysis

To investigate the connectivity between neurons, Transfer Entropy (TE) was utilized. TE is a computation technique that allows us to measure the interaction between two times series: a source series I and a target series J. TE is positive if it includes information about neuron I's spiking activity which improves the

prediction of neuron J's spiking activity beyond the prediction based on neuron J's past alone.
In our analysis, we embedded multiple time bins to capture temporal dependencies effectively. To account for synaptic delays between neurons, we adopted a robust methodology, which involves employing multiple bins of past history in the TE computation and considering message length greater than one bin [7]. By doing so, we enhanced the accuracy of predicting the effective connectivity between neurons using discrete time series. The equation for TE, considering multiple time delays and message length, is given by:

$$TE_{I\to J(d)} = \sum_{j_t, j_{t-1}, i_{t-1}} p(j_t, j_{t-1}^k, i_{t-d}^l) log_2(\frac{p(j_t|j_{t-1}^k, i_{t-d}^l)}{p(j_t|j_{t-1}^k)}) \tag{6}$$

where d: multiple time delays from 0 to 20 ms, k: number of bins of history from the receiver considered, and I: number of bins of history from the sender considered.

3.4.2 Firing rates method

As we know, spikes are generated and propagate along the axon of the cell toward the synapses of other neurons. We consider a stimulus, which will result in a certain train of spikes, modeled as a sequence of instantaneous impulses:

$$\rho(t) = \sum_{i=1}^{n} \delta(t - t_i) \tag{7}$$

where $\rho : [0, T] \to R$ is called the neural response function. We can find the spike count rate as the average rate of spikes:

$$r = \frac{n}{T} = \frac{1}{T} \int_0^T (d\tau \rho(\tau)) \tag{8}$$

By running the a moving average instead, we can define the time independent firing rate as:

$$r(t) = \frac{1}{\Delta t} \int d\tau < \rho(\tau) >$$

where the average path $< \rho(\tau) >$ is an ensemble average. In practical, r(t) can be measured by discretizing time with time-step Δt, counting the spikes in each time interval and normalizing:

$$r(t) = \frac{Spikes/bin}{\Delta t} \tag{9}$$

3.4.3 Coincidence analysis

In our investigation, the focus resided upon the discernment of coincident firing patterns within the ensemble of neurons. This analytical pursuit, known as coincidence analysis, was meticulously executed as a pivotal facet of our study. At its core, the principle underpinning coincidence analysis entails the meticulous comparison of temporal spike occurrences among a cohort of neurons, comprising a substantial 100 neurons in our specific case. This methodological endeavor hinges upon the scrutiny of spike timings derived from disparate neurons. When these spikes manifest within a confined temporal proximity, an indication arises that these neurons are engaged in a synchronized firing state, colloquially referred to as coincidence. To unravel these synchronicities, we adeptly employed the technique of cross-correlation. The crux of our approach lies in the calculation of cross-correlation, an analytical tool that quantifies the likelihood of a spike's occurrence within a predefined time window subsequent to the appearance of a spike in a distinct neuron. Through this mechanism, we discerned and substantiated the presence of concurrent neuronal firing patterns, thereby contributing to a more profound comprehension of the underlying dynamics of neural ensembles.

3.4.4 Null models

3.4.4.1 Null models for TE

While TE is a distinguished technique to infer the effective connectivity, it is bivariate in nature and comes with certain limitations that require additional measures to ensure the robust analysis. To deal with that problem, the null model was introduced [16]. With the Monte Carlo approach, we created a null model by jittering spike times solely from the sender neuron, thereby preserving the receiver neuron's auto-prediction ability. This null model ensured that the firing rate remained intact while introducing random temporal correlations between

spikes in the two times series. To achieve this, each spike in the source series was jittered using a Gaussian distribution centered on the actual spike time with a standard deviation of 10ms, resulting in a stringent analysis.

3.4.4.2 Null models for coincidence analysis

Neurons can exhibit correlated firing patterns, leading to the perception of synchronous activity or coincidences. However, these coincidences may not be indicative of true functional connections or interactions between neurons. Instead, they could be a result of random spike timing fluctuations. In order to debate this issue, we performed the null models for coincidence analysis to make sure there is no synchronization. By generating random shifts to the spike time of the data, we aimed to assess whether the observed synchronous firing patterns among neurons were indeed a product of genuine functional connections or merely a consequence of chance-based spike timing fluctuations. This evaluation allowed us to discern between meaningful neural interactions and random coincidences.

3.4.5 Gaussian filter

The Gaussian filter stands out as a highly potential instrument for effecting data filtration, image manipulation, and computational visual perception. The Gaussian filter affords the capacity to reduce the signal noise and enhance the accuracy of the dataset. In our study, we employed the Gaussian filter analysis to simulate spike time, both non bursty and bursty spike patterns, as well as to actual spiking data from cultured neurons. This application culminated in an improved data representation, thereby facilitating more refined analytical examination. The Gaussian filter algorithms we used are based on the basis of Hodson's work [6]. The one-dimensional Gaussian can be mathematically formulated as follow:

$$G(\tau) = \frac{1}{\sqrt{2\pi\sigma}} exp(\frac{-\tau^2}{\sigma^2}) \tag{10}$$

where $G(\tau)$ represents a convolution filter applied to the spike train, serving the purpose of signal smoothing. σ denotes the variance of the Gaussian filter, and the magnitude of the filter kernel l can be determined by excluding values that fall between 5% of the maximum kernel value. The two-dimensional Gaussian formulation is expressed as:

$$G(x,y) = \frac{1}{\sqrt{2\pi\sigma}} exp(\frac{-(x+y))^2}{\sigma^2}) \tag{11}$$

This representation offers the means to apply Gaussian smoothing in two dimensions, enabling refined data manipulation in various contexts, where $-x \leq l$ and $l \leq y$.

Chapter 4

Results

4.1 Non-bursty simulated data

The simulated data was produced using the Izhikevich model (§3.1) implemented in Python. Within this simulated dataset, two types of spike patterns were generated: bursty spike data and non-bursty spike data. The Intrinsically Bursting regime was characterized by assigning maximum and minimum weights of 15 and 5, respectively, for excitatory connections, while the maximum and minimum weights for inhibitory connections were set at 2. On the other hand, for the non-bursty spike data, the maximum and minimum weights for excitatory connections were 10 and 0, respectively, and the maximum and minimum weights for inhibitory connections were 5.
We first consider simulations in the non bursty regime. In Figure 3A we show the raster plot of an activity snapshot of 5s. It is immediately apparent that a few neurons spike with considerably increased frequency with respect to the others. These are all inhibitory neurons that, due to the absence of inhibitory-inhibitory connections in our simulation, tend to present higher spiking rates. This is further analyzed in Figure 3B, which presents the distribution of 100 spikes rates. Typical rates of excitatory neurons are of the order of 0.005 kHz (5 Hz), while a few inhibitory neurons present rates up to 0.16 kHz (160Hz).

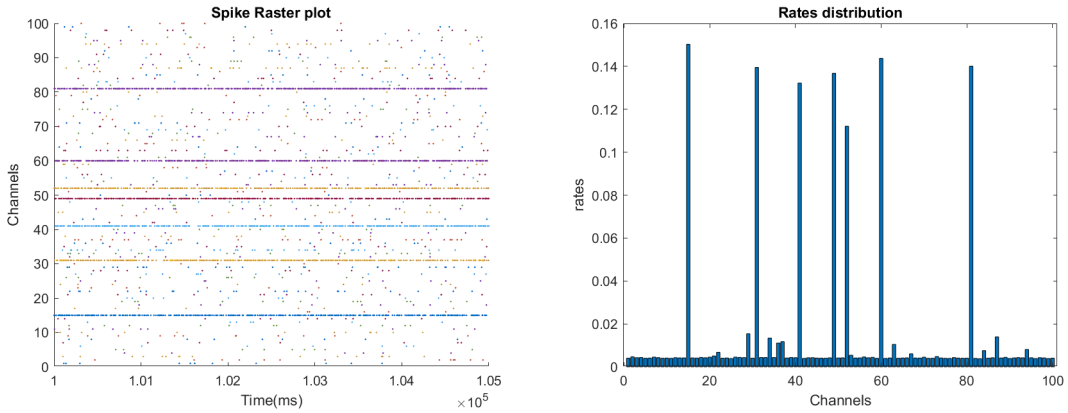

(A) (B)

Figure 3: The neuron raster plot for non bursty simulated spike: (A) Spiking activity of simulated non bursty 100 neurons for 5s. (B) The spike rate distribution of 100 simulated non bursty neurons.

4.1.1 TE analysis and null models

The first connectivity metric analyzed is transfer entropy (TE). TE yields insights into how much information from one neuron's activity can influence the activity of another neuron. We first computed TE values with delays from 1 to 20, and then kept a unique TE value corresponding to the maximum TE across delays. Raw TE values were later subjected to a null model testing (§3.4.4) at the level of each connection to identify significant links. The significance of each connection is computed by iterating 1000 null models by jittering spike times solely from the sender neuron, computing a threshold corresponding to the upper 0.005 tail of the distribution, and keeping connections above threshold [10]. Results are summarized in Figure 4A and 4B, respectively, where we show the matrices for the raw and significance-corrected TE, respectively. The values of TE span 3 orders of magnitude (roughly $10^{-}5$ to $10^{-}2$). The corresponding distributions are shown in Figure 5. Both before and after correction, the distributions are unimodal, with a central peak underscoring the prevalence of a dominant connectivity strength. Notably, the effect of the null model is not just that of generally removing weak connections, as a unique threshold across all neurons would do. In fact, spurious connections may arise with considerably different strengths, depending on the spike rates of the pair of neurons considered.

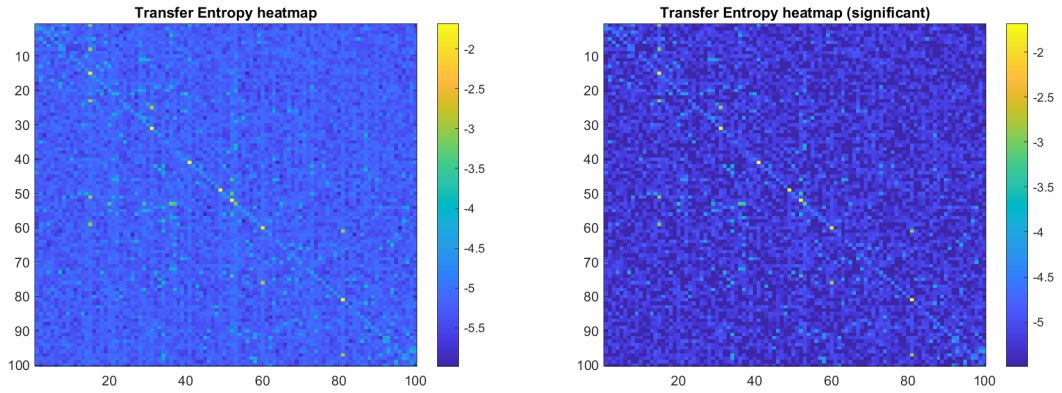

(A) (B)

Figure 4: TE heat map: (A) Heat map of simulated non bursty spike TE. (B) Heat map of simulated non bursty spike TE with significance.

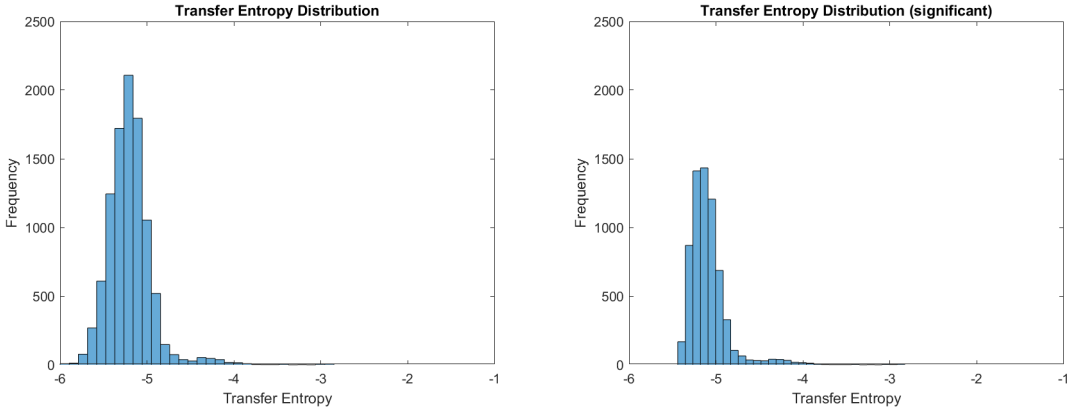

(A) (B)

Figure 5: TE distribution: (A) Distribution of simulated non bursty spike TE. (B) Distribution of simulated non bursty spike TE with significance (The significance is computed by iterating 1000 null models by jittering spike times solely from the sender neuron with 5% threshold).

The configuration of the neuronal network is elucidated in Figure 6A and 6B, where links are drawn based on TE and significant-TE values, respectively.

In Figure 7 we assess to what extent TE matches the ground-truth connectivity (GTC) between neurons. To this aim, we show a scatter plot of TE vs. GTC. We observed a positive correlation, as evidenced by the Pearson correlation coefficient of R = 0.32: as connectivity values increase, TE values tend to increase as well, though the relationship is not particularly strong. However, this global value of correlation is significantly affected by negative inhibitory-excitatory connections (which must yield positive TE, as in principle TE is sensitive to the magnitude of interaction, not its sign) and null inhibitory-inhibitory connections. In Figure 7B, we explicitly separate the contribution of four types of connections: inhibitory to excitatory (IE) inhibitory to inhibitory (II), excitatory to inhibitory (EI) and excitatory to excitatory (EE). Correspondingly, we computed the value of TE-GTC Pearson correlation for each class (except the II class, for which the correlation is undefined as all II ground-truth connections are null). The EE and EI classes gave a Pearson correlation of R = 0.50 and R = 0.67, considerably better than the previously reported global value. In contrast, the association in the IE class was much weaker (R = -0.04). In summary, TE can reconstruct fairly well EE and EI connections, while it fails to detect IE connections and detects many spurious II connections.

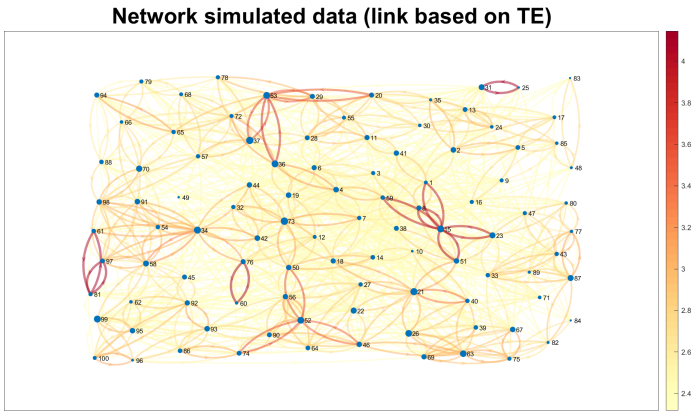

(A)

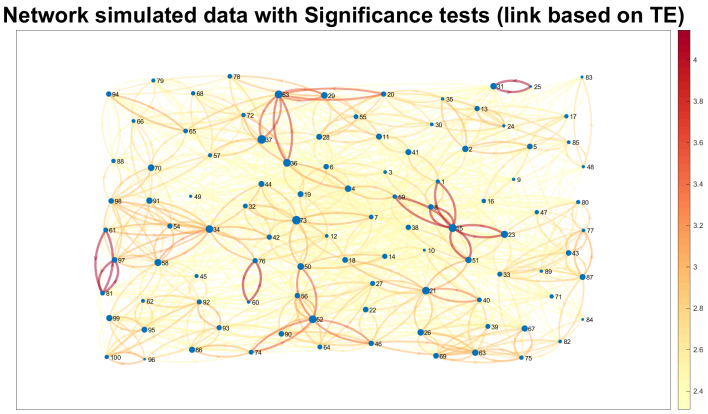

(B)

Figure 6: Neuronal network: (A) The neuronal network with the link based on simulated non bursty spike TE. (B) The neuronal network with the link based on simulated non bursty spike TE with significance (The significance is computed by iterating 1000 null models by jittering spike times solely from the sender neuron with 5% threshold).

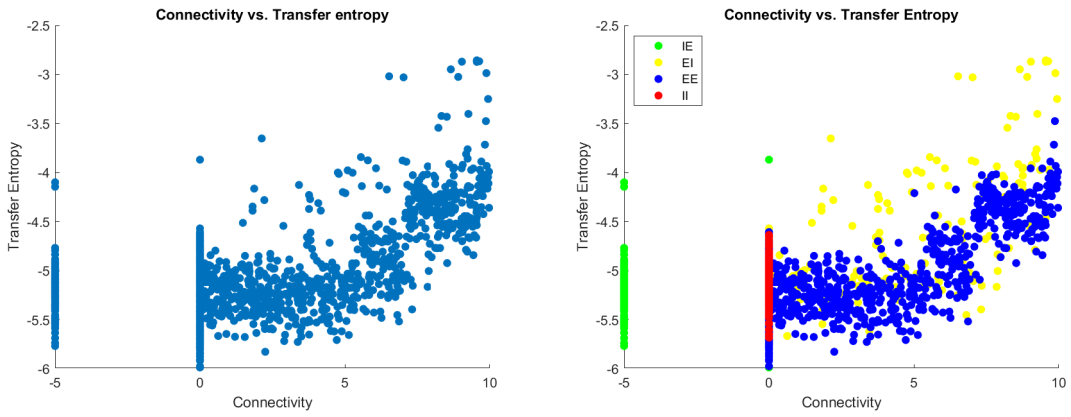

(A) (B)

Figure 7: Connectivity and TE: Scatter plot between simulated non bursty spike time connectivity and TE values. (B) Scatter plot between simulated non bursty spike time connectivity and TE values with 4 kinds of connectivities, IE: inhibitory to excitatory connectivity, II: inhibitory to inhibitory connectivity, EI: excitatory to inhibitory connectivity, EE: excitatory to excitatory connectivity.

4.1.2 Coincidences analysis and null models

The second connectivity metric we consider is the number of spiking coincidences (NSC) within the same window or within two successive windows (delay 0 and delay 1, respectively). The coincidence matrices for the two delays are shown in Figure 8. It is immediate to notice that the two matrices are highly similar and both dominated by the high-rate (HR) neurons, which exhibit many coincidences both among themselves and with other, low rate (LR) neurons in the network. In Figure 9 we analyze the distribution of the number of coincidences. From Figure 9A, where we show the distribution for delay 0, it is evident that the distribution is trimodal: the three peaks simply correspond to the HR-HR, HR-LR and LR-LR coincidences. A similar pattern is observed with a temporal delay of 1 (Figure 9B).

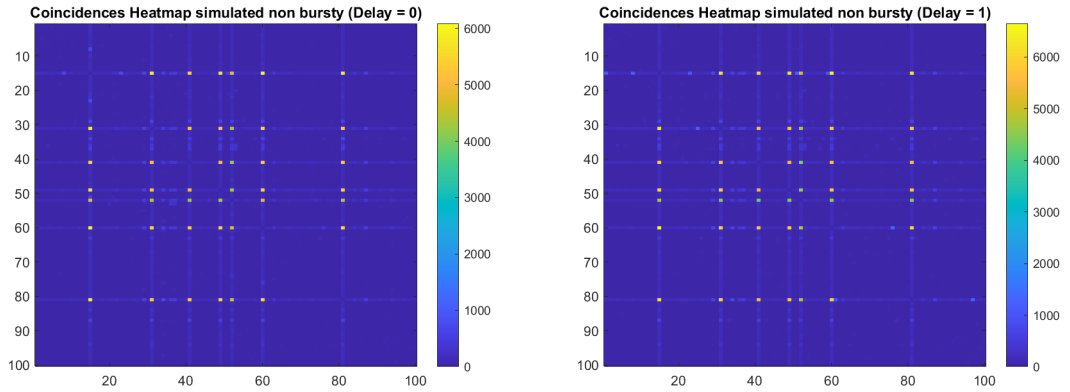

(A) (B)

Figure 8: Coincidences heatmap: (A) The coincidences heat map of simulated non bursty spikes for 100 neurons at delay 0. (B) The coincidences heat map of simulated non bursty spikes for 100 neurons at delay 1.

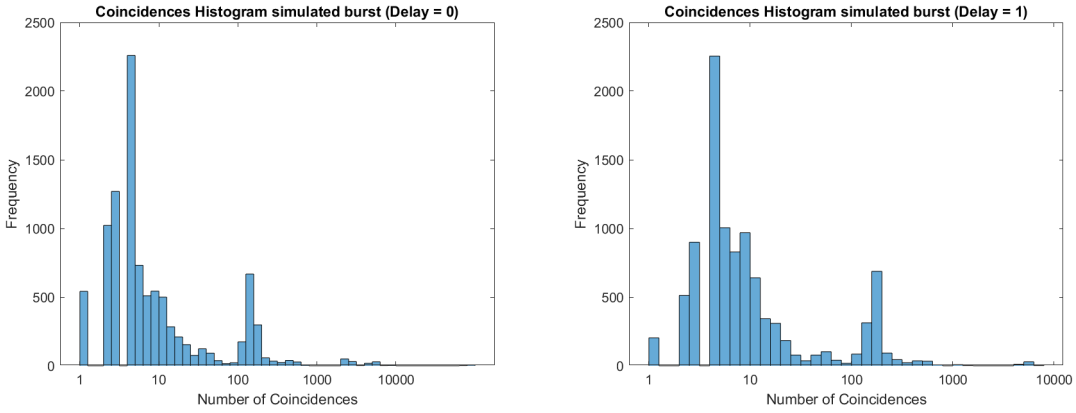

(A) (B)

Figure 9: Distribution of coincidences: (A) The coincidence distribution of simulated non bursty spikes for 100 neurons at delay 0. (B) The coincidence distribution of simulated non bursty spikes for 100 neurons at delay 1.

The relationship between significant coincidental events, across both temporal delays, and ground truth connectivity is presented in Figure 10. The average Pearson correlation is virtually null, R = -0.01 for delay 0 and R = 0.01 for delay

1. Again, the global values conceal the different contributions by different connection types. Differentiating between the four distinct categories of neuronal connectivity, we find a high correlation for the EE class, R = 0.73 for delay 0 and R = 0.85. For the EI class, we find a much weaker correlation, R = 0.24 for delay and R = 0.36 for delay 1. In particular, we observe that EI connections tend to be overestimated. This is probably the consequence of a large number of spurious coincidences due to the very large spiking rate of inhibitory neurons. This also creates a very large number of spurious coincidences in the II class and the IE class.

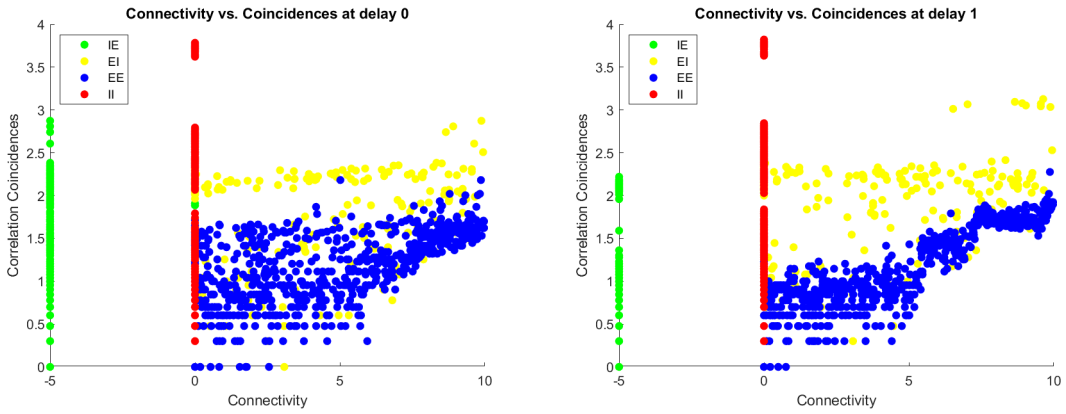

(A) (B)

Figure 10: Connectivity and coincidence: (A) Scatter plot between simulated non bursty spike time connectivity and coincidences values at delay 0 (B) Scatter plot between simulated non bursty spike time connectivity and coincidences values at delay 1.

To possibly control for spurious coincidences, we decided to normalize the number of coincidences by removing the number of coincidences that would be expected purely on the basis of the two neurons' spike rates. For a neuron with spike rate r, the number of expected events in a window of length L is simply rL. Thus for two completely independent neurons with rates r_1 and r_2, the expected number of coincidences in a window of time L is $r_1 r_2 L^2$. In a total of M time windows, the expected number of coincidences is $E_{1,2} = r_1 r_2 L^2 M$. We defined a "normalized" number of coincides between neurons i and j given by

$$\tilde{N}_{i,j} = \frac{N_{i,j} - E_{i,j}}{E_{i,j}} \tag{12}$$

where $N_{i,j}$ is the observed number of coincidences. Figure 11 portrays the relation between the ground-truth connectivity and the normalized coincidences. We can observe that the normalization is effective in mitigating, if not curing, the spurious effects described above. As a result, the global e GTC-NSC correlation achieves a value of R = 0.60 for delay 0 and R = 0.79 for delay 1. For the EE class, the GTC-NSC correlation increases up to R = 0.76 for delay 0 and R = 0.87 for delay 1. For the EI class, the effect of spurious coincidences is considerably attenuated and one obtains a GTC-NSC correlation of R = 0.74 for delay 0 and R=0.80 for delay 1. In addition, the delay-1 coincidences can correctly identify the negative connections in the IE class, as most of these connections are correctly associated with a negative number of normalized coincidences (correctly, when an inhibitory neuron spikes, in the number of spikes of a down-stream excitatory neurons is less likely than what would be expected randomly. Finally, the II class yields very low values of normalized coincidences, so that one does not detect strong spurious II connections.

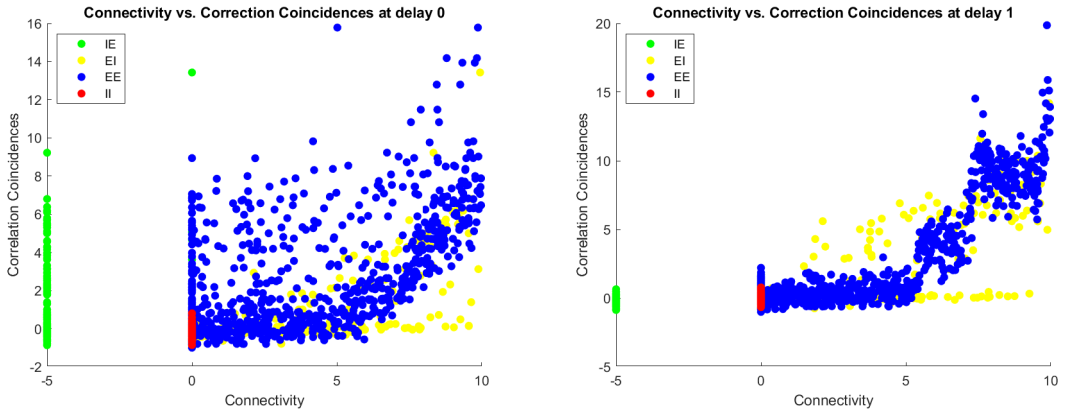

(A) (B)

Figure 11: Connectivity and coincidence: (A) Scatter plot between simulated non bursty spike time connectivity and normalized coincidences values at delay 0 (B) Scatter plot between simulated non bursty spike time connectivity and coincidences values at delay 1.

We compare this analysis to the outcomes of a more standard null model test. a circular-permutation based significance test for coincidences (§3.4.4.2). This test also removes many spurious coincidences (Figure 12). Unsurprisingly, when looking at the distribution of coincidences (Figure 13), we observe that the distribution has become unimodal, as the high number of spurious II and IE coincidences have been removed by the null model testing.

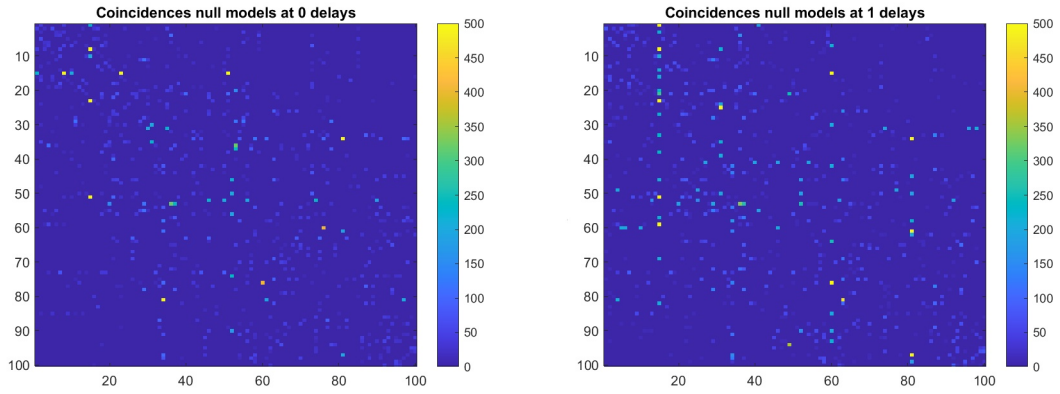

(A) (B)

Figure 12: Coincidences heatmap: (A) The coincidences of non bursty spikes with significance (The significance is computed by iterating 1000 null models by applying random shift to the spike times to the data with 5% threshold) heat map of simulated non bursty spikes for 100 neurons at delay 0. (B) The coincidences of non bursty spikes with significance (The significance is computed by iterating 1000 null models by applying random spike times to the data with 5% threshold) heat map of simulated non bursty spikes for 100 neurons.

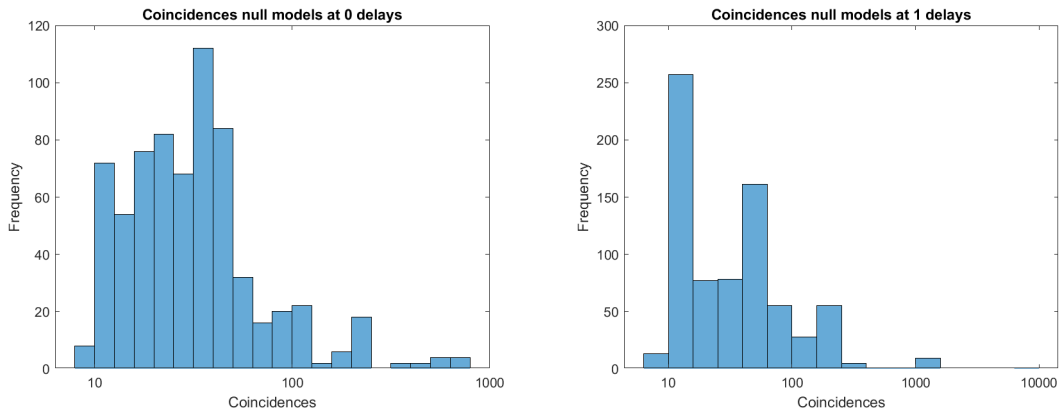

(A) (B)

Figure 13: Distribution of coincidences: (A) The coincidences with significance (The significance is computed by iterating 1000 null models by applying random spike times to the data with 5% threshold) distribution of simulated non bursty spikes for 100 neurons at delay 0. (B) The coincidences with significance (The significance is computed by iterating 1000 null models by applying random spike times to the data with 5% threshold) of simulated non bursty spikes for 100 neurons at delay 1.

In Figure 14 we compare the significant coincidences with the ground truth connectivity at delays 0 and 1. Results are much better than without correction, with global values of GTC-NSC correlation of R = 0.2396 for delay 0 and and R = 0.18293 for delays 1. Specifically, the functional roles of individual connectivity types are elucidated as in previous cases. Within the EE and EI classes we have a sizable improvement in correlation, evidenced by correlation coefficients of R = 0.75 and R = 0.59 for delay 0, as well as R = 0.87 and R = 0.52 for delay 1. Conversely, the spurious IE and II coincidences appear comparatively diminished.
Figures 15 and 16 show us the structural configuration of the simulated non-bursty neuronal network, with links reconstructed using non-normalized and normalized coincidences. respectively. Figure 15 is completely dominated by high-rate neurons, which form strong links with all other neurons in the network. Notably, Figure 16 effectively illustrates the network's coherent linkage and its propensity to organize into discernible clusters (for both delay settings).

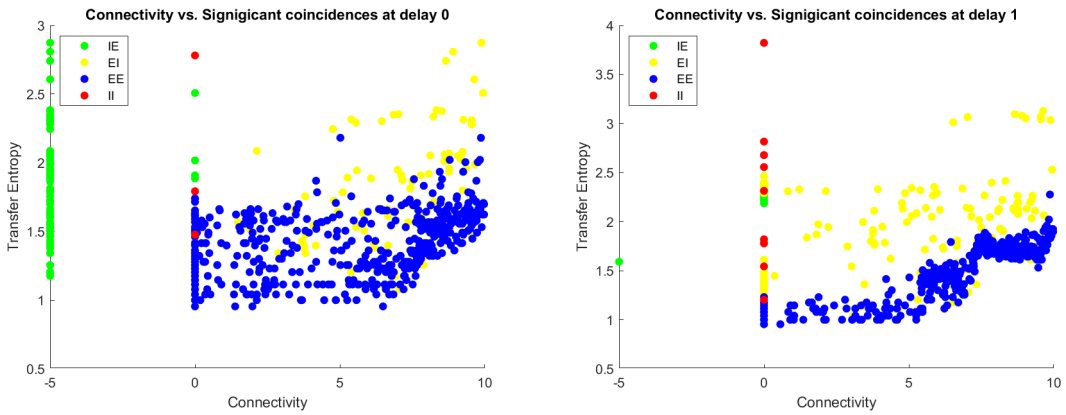

(A) (B)

Figure 14: Connectivity and coincidence: (A) Scatter plot between simulated non bursty spike time connectivity and coincidences with Significance test at delay 0. (B) Scatter plot between simulated non bursty spike time connectivity and coincidences with Significance test at delay 1.

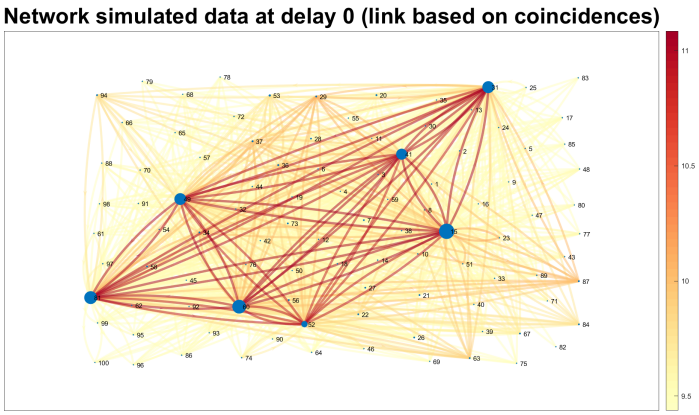

(A)

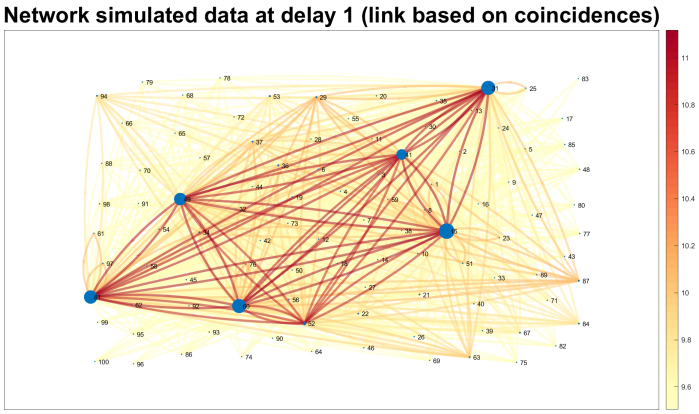

(B)

Figure 15: Neuronal network: (A) The neuronal network with the link based on simulated non bursty spike Coincidence at delay 0. (B) The neuronal network with the link based on simulated non bursty spike Coincidence at delay 1.

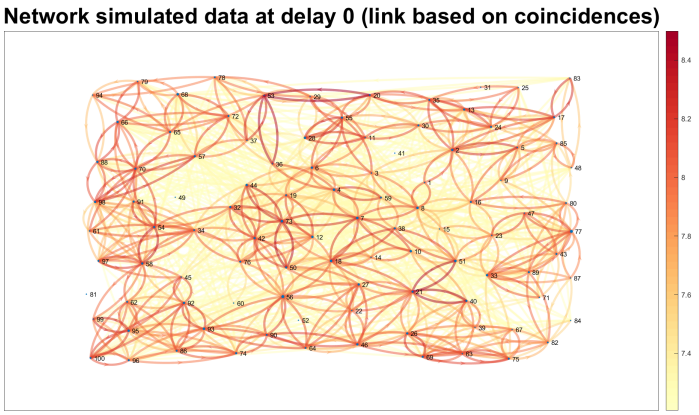

(A)

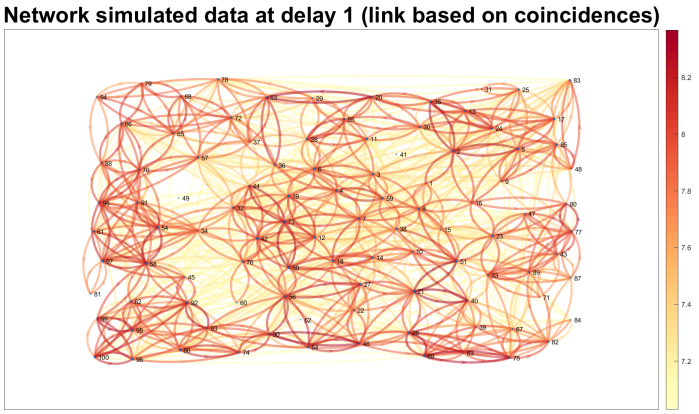

(B)

Figure 16: Neuronal network: (A) The neuronal network with the link based on simulated non bursty normalized coincidences at delay 0. (B) The neuronal network with the link based on non bursty simulated normalized coincidences at delay 1.

4.1.3 Gaussian filter analysis

The final connectivity metric we consider is just the standard Pearson correlation of the smoothed time series, which in neuroscience is commonly referred to as "functional connectivity" [9]. To this aim, we first applied a Gaussian filter to

the spike time series and then computed the Pearson correlation. We tried two different values of the filter width (10 ms and 100 ms respectively). Figure 17 shows the outcomes of the Gaussian filter analysis applied to a snapshot of one simulated time series. The illustration effectively demonstrates the noise-filtering impact of the Gaussian filter on the spike signal. The effective of Gaussian filter with 2 different filters can be represent perspicuously with 2 different heat map in Figure 18.

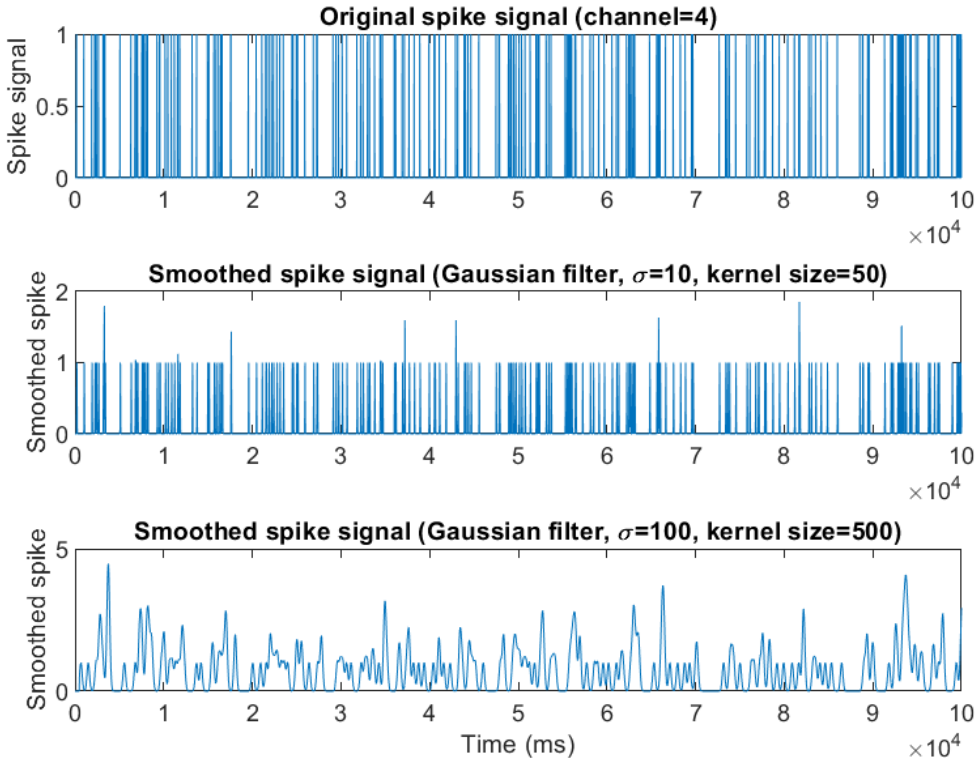

Figure 17: Gaussian filter: The application of a Gaussian filter to the simulated non bursty spike data using two different filter standard deviation values: $\sigma = 10$ and $\sigma = 100$.

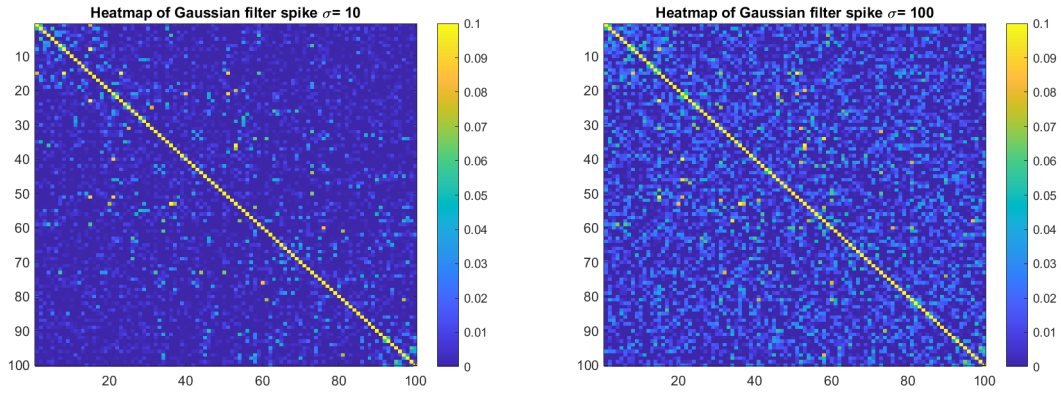

(A) (B)

Figure 18: Coincidences heatmap: (A) The heatmap of Guassian filter for simulated non bursty spike at $\sigma = 10$. (B) The heatmap of Guassian filter for simulated non bursty spike at $\sigma = 100$.

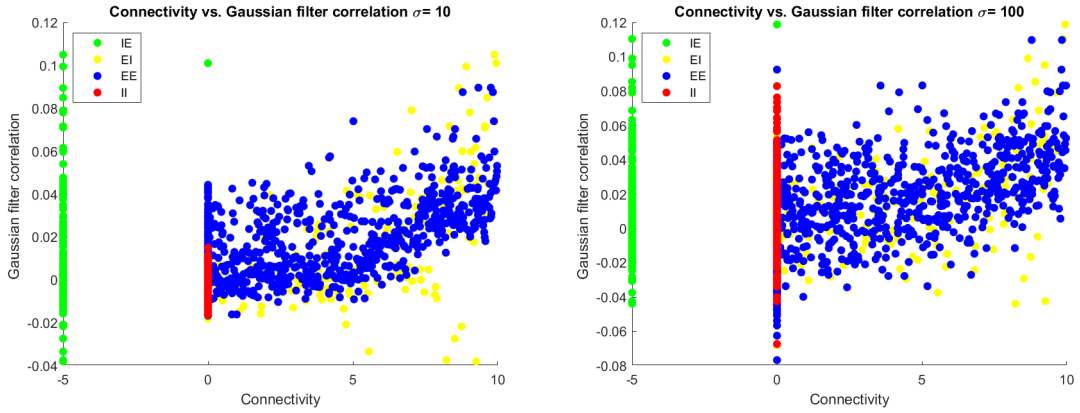

(A) (B)

Figure 19: Connectivity and Gaussian filter correction: (A) Scatter plot between simulated non bursty spike time connectivity and Gaussian correction at $\sigma = 10$. (B) Scatter plot between simulated non bursty spike time connectivity and coincidences with Significance test at $\sigma = 100$.

Figure 19 presents a scatter plot depicting the association between ground-truth connectivity and functional connectivity following the application of Gaus-

sian filters. A discernible pattern emerges in both plots, revealing a favorable association between connectivity and spikes subjected to Gaussian filtration. We see a lower filter standard deviation ensures a larger degree of association. Globally, the GTC-FC correlation is R = 0.48 for $\sigma = 10$ and R = 0.25 for $\sigma = 100$. Splitting the contributions of various connectivity types, we see that the EE and EI classed have high values of correlation, R = 0.69 for EE and R = 0.60 for EI for $\sigma = 10$ (only 0.37 for EE and 0.32 for EI in the case of $\sigma = 100$). In addition, the FC values are generally weak for spurious II connections. Conversely, IE connections exhibit generally non-negligible values of FC, with a correlation coefficient of R = -0.36 for $\sigma = 10$ (R = -0.19 for $\sigma = 100$).

4.1.4 Summary

In summary, we tested three metrics (transfer entropy, TE; number of spiking coincidences, NSC; Gaussian filter functional connectivity, FC) in their ability to reconstruct the true connectivity structure of the network. For NSC we used two values of delay (0 delay and one window of delay, corresponding to a delay of 10 ms). For FC; we used two values for the filter standard deviations ($\sigma = 10ms$ and $\sigma = 100ms$).
TE, normalized NSC and FC all achieved some degree of success in reconstructing the network. However, the methods' performances highly depend on the type of connection. TE and FC assign strong links to some of the spurious II connections. This problem is minimized by NSC (upon normalization), especially at delay 1. EE connections are well detected by all methods (very well by normalized NSC). IE connections are identified by all methods, but FC and TE are not able to spot the inhibitory nature of these connections. Only normalized NSC at delay 1 can, to a fair extent, identify this feature. Finally, all methods identify EI connections, although not as well as EE connections.
Overall, the best method among those tested is normalized NSC with delay.

4.2 Bursty simulated data

Next, we repeated the analyses in §4.1 on simulations involving bursty neuronal spiking patterns. This case is more difficult than the non-bursty one, for at least two reasons. Firstly, bursts tend to cause multi-neuron coincidence events; these events significantly raise the number of coincidences occurring between neurons

that are not directly connected. Stated otherwise, bursty dynamics significantly enhances network effects depending on indirect connections. As all connectivity reconstruction methods used are bivariate, they cannot easily discriminate between direct and indirect effects. Secondly, the presence of bursts, a collective phenomenon, makes it difficult to generate accurate null models removing the specific effect of a given connection, as most null models cannot preserve bursts. Figure 20A represents the raster plot depicting bursty spiking events. Figure 20B shows the distribution of spike rates. Again, inhibitory neurons have a large spike rate. Most excitatory neurons have an average rate of 0.005 kHz (5 Hz), in line with the non-bursty simulation.

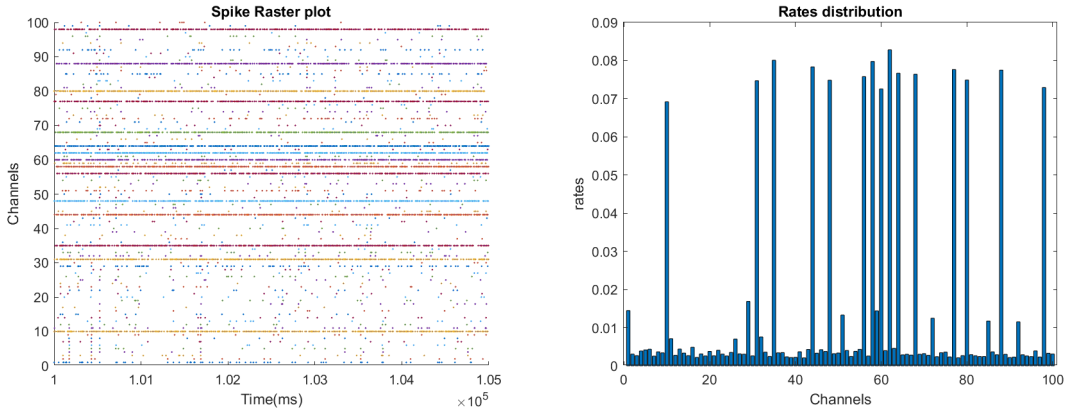

(A) (B)

Figure 20: The neuron raster plot for bursty simulated spike: (A) Spiking activity of simulated 100 bursty neurons for 5s. Each neuron within an assembly bursts at high frequency. (B) The spike rate distribution of 100 simulated neurons with rates.

4.2.1 TE analysis and null models

The initial metric examined for the analysis of bursty neuronal spiking patterns is transfer entropy (TE), similar to our analysis of the non-bursty regime. TE values are computed with delays ranging from 1 to 20. A single TE value is then retained, corresponding to the highest TE value among the various delays. Subsequently, the raw TE values undergo testing using a null model (as already detailed in §3.4.4 and §4.1) on a per-connection basis. The findings are sum-

marized in Figure 21A and 21B, presenting matrices for both the raw TE values and the TE values after significance correction. The range of TE values spans three orders of magnitude, approximately from 10^{-5} to 10^{-2}. The associated distributions are depicted in Figure 22. These distributions, both before and after correction, exhibit a single peak, but we also notice a fat tail, highlighting the presence of a core of strong links. The null model eliminates several links with strengths corresponding to the distribution peak, but it preserves links with strengths in the distribution tail. The configuration of the neuronal network is clarified in Figure 23A and 23B, where connections are depicted based on TE and significant-TE values, respectively.

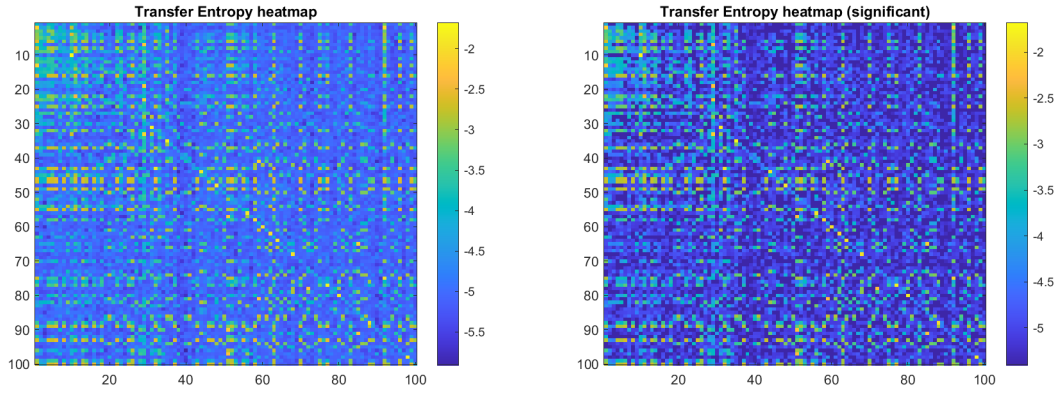

(A) (B)

Figure 21: TE heat map: (A) Heat map of simulated bursty spike TE. (B) Heat map of simulated bursty spike TE with significance.

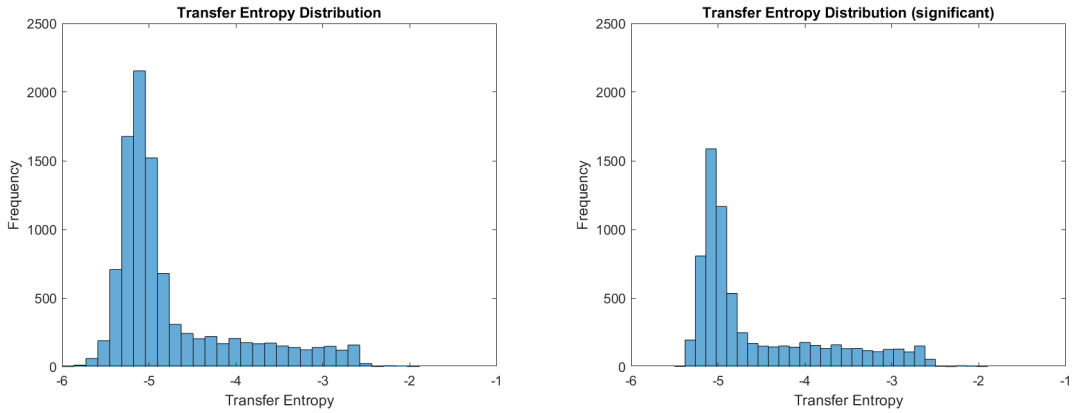

(A) (B)

Figure 22: TE distribution: (A) Distribution of simulated bursty spike TE. (B) Distribution of simulated bursty spike TE with significance (The significance is computed by iterating 1000 null models by jittering spike times solely from the sender neuron with 5% threshold).

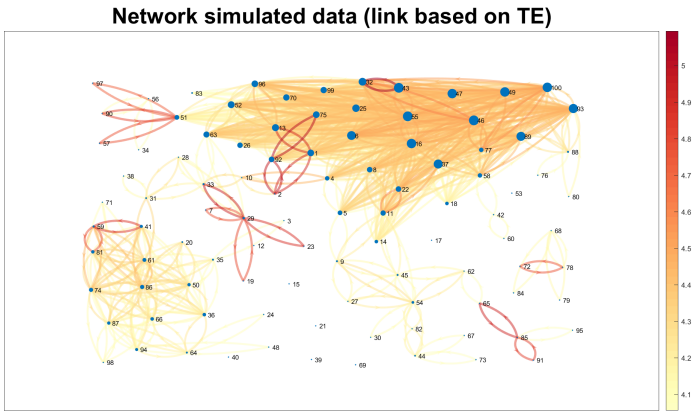

(A)

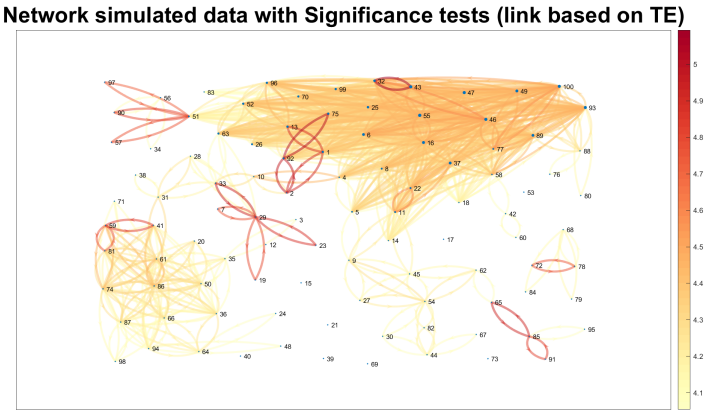

(B)

Figure 23: Neuronal network: (A) The neuronal network with the link based on simulated bursty spike TE. (B) The neuronal network with the link based on simulated bursty spike TE with significance (The significance is computed by iterating 1000 null models by jittering spike times solely from the sender neuron with 5% threshold).

In Figure 24, we investigate the degree to which TE aligns with GTC among neurons. For this purpose, we present a scatter plot illustrating TE against GTC. Our observations reveal a positive correlation, indicated by the Pearson correlation coefficient of R = 0.45. However, it is important to note that this overall

correlation value is significantly influenced by negative IE connections, which inherently result in positive TE values due to TE's sensitivity to interaction magnitude rather than its polarity. Additionally, null II connections can also impact this correlation. In Figure 24B, we explicitly disentangle the contribution of four distinct connection types: IE, II, EI, and EE. Correspondingly, we calculate the Pearson correlation coefficient for TE-GTC for each connection class (excluding the II class, where correlation is undefined since all II ground-truth connections are null). The EE and EI classes yield Pearson correlations of R = 0.60 and R = 0.36, respectively, which are notably better than the previously reported overall correlation. On the contrary, the correlation within the IE class is notably weaker (R = -0.09). In summary, TE exhibits a fairly accurate reconstruction of EE connections, a poorly accurate detection of EI connections, while it struggles to detect IE connections and tends to identify numerous erroneous II connections.

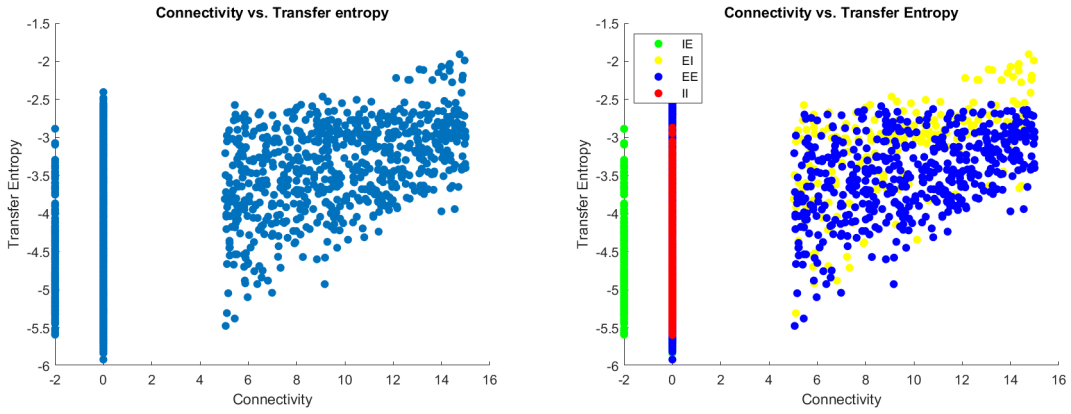

(A) (B)

Figure 24: Connectivity and TE: Scatter plot between simulated bursty spike time connectivity and TE values. (B) Scatter plot between simulated bursty spike time connectivity and TE values with 4 kinds of connectivities, IE: inhibitory to excitatory connectivity, II: inhibitory to inhibitory connectivity, EI: excitatory to inhibitory connectivity, EE: excitatory to excitatory connectivity.

4.2.2 Coincidences analysis and null models

We turn our attention to the second connectivity metric in our analysis, NSC. The matrices illustrating coincidences for these two time delays are presented in

Figure 25. As in §4.2.1, the two matrices have a striking degree of similarity, being equally influenced by the presence of HR neurons, which display numerous coincidences both internally among themselves and externally with LR neurons within the network. Shifting our focus to Figure 26, we delve into the examination of coincidence count distributions. In Figure 26A, depicting the distribution for delay 0, a trimodal nature becomes evident. These three distinct peaks correspond to the coincidences involving HR-HR, HR-LR, and LR-LR neuron pairs. A comparable pattern emerges when considering a temporal delay of 1, as depicted in Figure 26B.

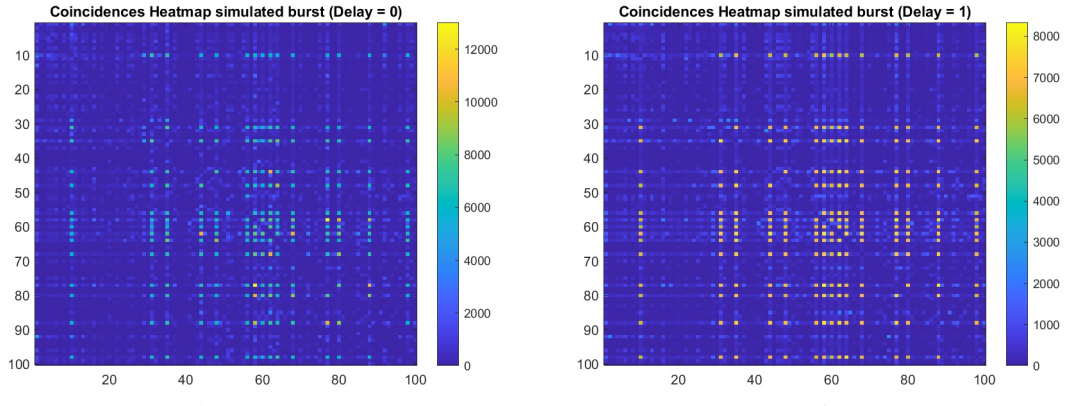

(A) (B)

Figure 25: Coincidences heatmap: (A) The coincidences heat map of simulated bursty spikes for 100 neurons at delay 0. (B) The coincidences heat map of simulated bursty spikes for 100 neurons at delay 1.

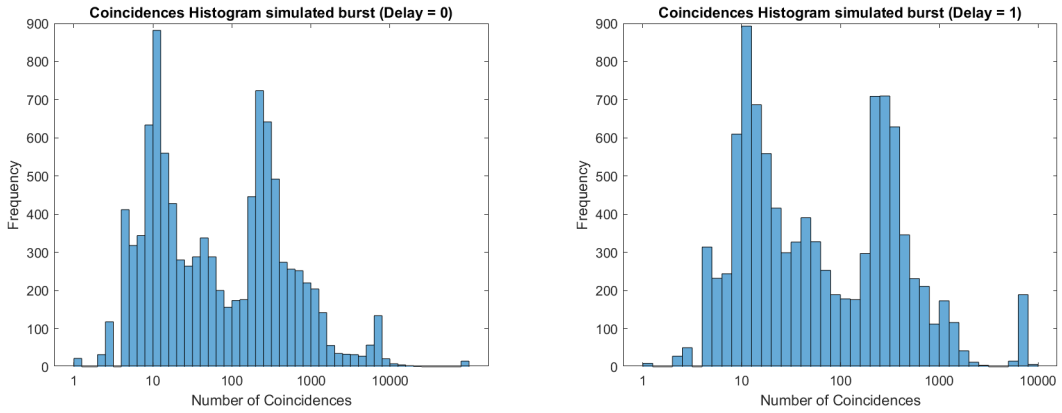

(A) (B)

Figure 26: Distribution of coincidences: (A) The coincidence distribution of simulated bursty spikes for 100 neurons at delay 0. (B) The coincidence distribution of simulated bursty spikes for 100 neurons at delay 1.

Figure 27 illustrates the connection between significant coincidental events occurring at different temporal delays and the ground truth connectivity. The mean Pearson correlation is very weak: R = 0.06 for delay 0 and R = -0.02 for delay 1. However, these overall values obscure the varied contributions made by distinct types of connections. Within the EE class, a strong correlation is observed: R = 0.64 for delay 0 and R = 0.58 for delay 1. Furthermore, the EI class displays a stronger correlation, with R = 0.70 for delay 0 and R = 0.70 for delay 1. Notably, we notice a tendency for EI connections to be overestimated. This overestimation is likely due to a significant number of erroneous coincidences stemming from the notably high spiking rates of inhibitory neurons. This excessive coincidental activity also generates a substantial number of false coincidences within the II class and the IE class.

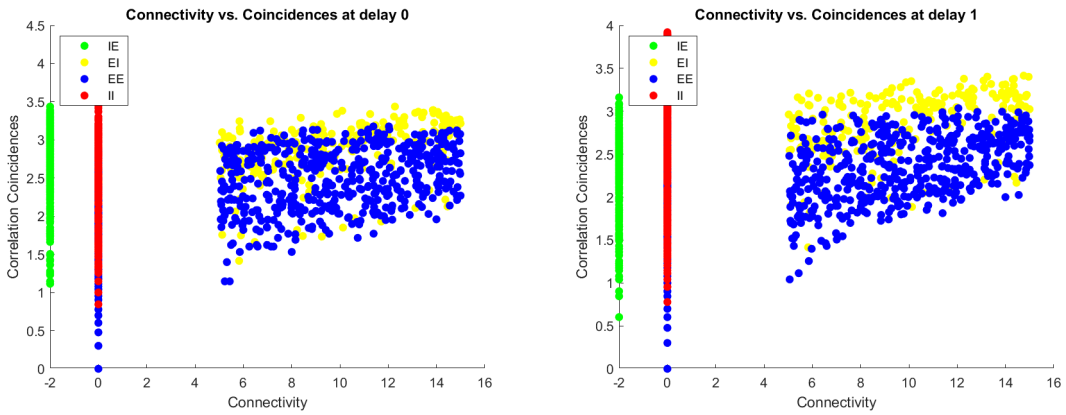

(A) (B)

Figure 27: Connectivity and coincidence: (A) Scatter plot between simulated bursty spike time connectivity and coincidences values at delay 0 (B) Scatter plot between simulated bursty spike time connectivity and coincidences values at delay 1.

Furthermore, the computation of adjusted coincidences was performed as expounded above in §4.1.2 (Figure 28). This figure depicts the correlation between ground-truth connectivity and normalized coincidences. Normalization improves the global correlation between GTC and NSC, which achieves a noteworthy value of R = 0.63 for delay 0 and R = 0.65 for delay 1. Within the EE class, the correlation between GTC and NSC is enhanced, reaching R=0.74 for delay 0 and R=0.69 for delay 1. However, the impact of erroneous coincidences within the EI class is not markedly dampened, resulting in a GTC-NSC correlation that is worse than what achieved before normalization: R = 0.57 for delay 0 and R = 0.57 for delay 1. Moreover, the coincidences at delay 1 cannot accurately identify negative connections within the IE class. Finally, the II class produces minimal values of normalized coincidences, effectively preventing the detection of substantial spurious II connections. Thus, contrary to the case of non-bursty dynamics, the process of normalization does not fully counteract the presence of spurious connections. This limited success is due to an inconsistency of the normalization procedure with the presence of bursts, a collective network phenomenon. In the presence of bursts, essentially all neurons, whether directly connected or not, tend to exhibit more coincidences than independent neurons.

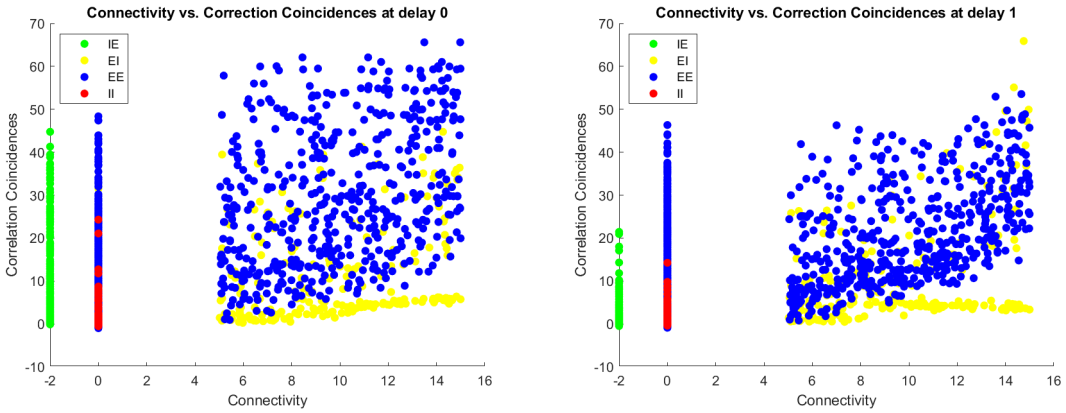

(A) (B)

Figure 28: Connectivity and coincidence: (A) Scatter plot between simulated bursty spike time connectivity and normalized coincidences values at delay 0 (B) Scatter plot between simulated bursty spike time connectivity and coincidences values at delay 1.

We continue to juxtapose this analysis with the results obtained from a more conventional null model examination, specifically a significance test for coincidences based on circular permutations (§3.4.4.2). This particular test contributes to the elimination of numerous erroneous coincidences. The coincidence pattern is no longer dominated by high-rate neurons (Figure 29A,B). In Figure 30 we present the distributions of coincident events, subjected to significance testing, for both delay settings. Contrary to distributions before testing, these distributions are nearly unimodal. This shift is attributed to the null model testing, which effectively eliminates the elevated count of spurious coincidences within the II and IE categories. Figure 31 presents a comparison between significant coincidental occurrences and the ground truth connectivity at both delay 0 and delay 1. The outcomes demonstrate a modest enhancement compared to the analysis without correction, yielding notable overall GTC-NSC correlation values of R = 0.16 for delay 0 and R = 0.20 for delay 1. In particular, the functional distinctions among various types of connectivity are once again clarified, mirroring the previous cases. Slight improvements in correlation are observed within the EE and EI classes, as shown by the correlation coefficients of R = 0.64 and R = 0.73 for delay 0, and R = 0.58 and R = 0.72 for delay 1. In contrast, the erroneous IE and II coincidences are not substantially reduced.

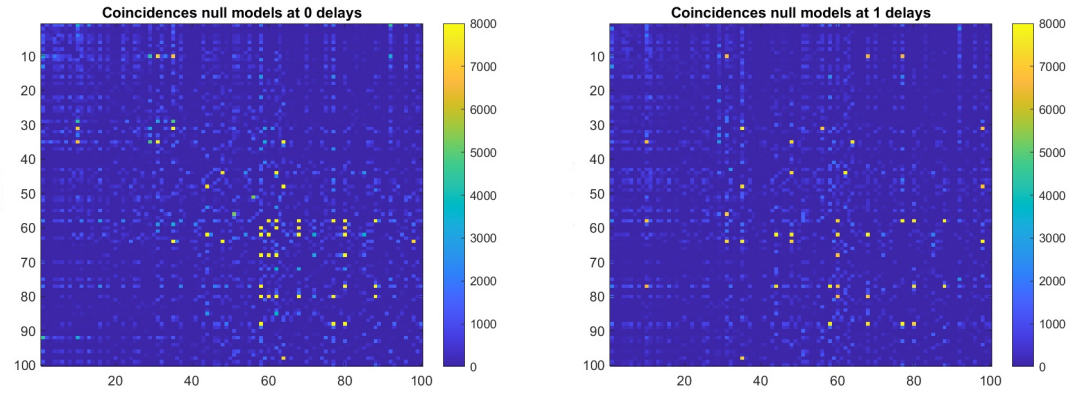

(A) (B)

Figure 29: Coincidences heatmap: (A) The coincidences of bursty spikes with significance (The significance is computed by iterating 1000 null models by applying random shift to the spike times to the data with 5% threshold) heat map of simulated non bursty spikes for 100 neurons at delay 0. (B) The coincidences of bursty spikes with significance (The significance is computed by iterating 1000 null models by applying random spike times to the data with 5% threshold) heat map of simulated non bursty spikes for 100 neurons.

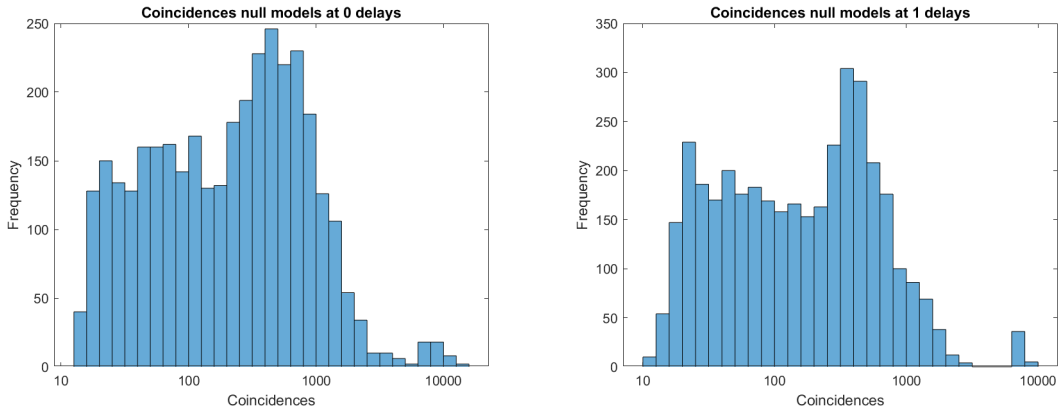

(A) (B)

Figure 30: Distribution of coincidences: (A) The coincidences with significance (The significance is computed by iterating 1000 null models by applying random spike times to the data with 5% threshold) distribution of simulated bursty spikes for 100 neurons at delay 0. (B) The coincidences with significance (The significance is computed by iterating 1000 null models by applying random spike times to the data with 5% threshold) of simulated bursty spikes for 100 neurons at delay 1.

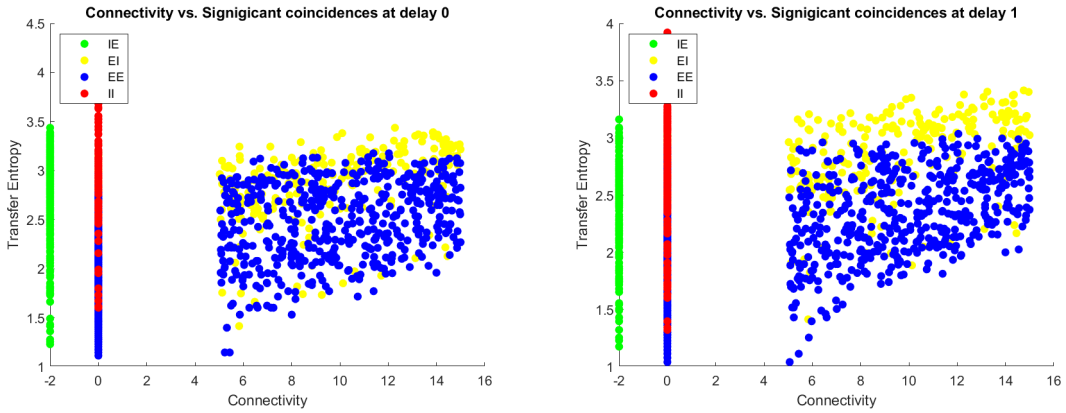

(A) (B)

Figure 31: Connectivity and coincidence: (A) Scatter plot between simulated bursty spike time connectivity and coincidences with Significance test at delay 0. (B) Scatter plot between simulated bursty spike time connectivity and coincidences with Significance test at delay 1.

Figures 32 and 33 offer insights into the structural arrangement of the simulated bursty neuronal network, showcasing link reconstruction through the utilization of non-normalized and normalized coincidences, respectively. Figure 32 is dominated by high-rate neurons, which form strong links with all other neurons in the network. This actually obscures a scenario where connections have a pronounced clustering, discernible in Figure 33.

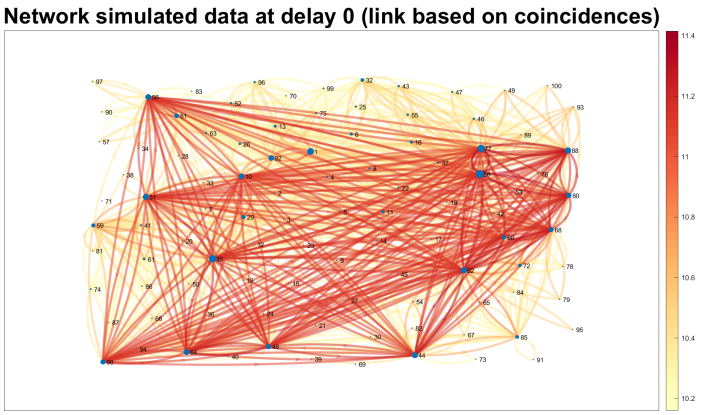

(A)

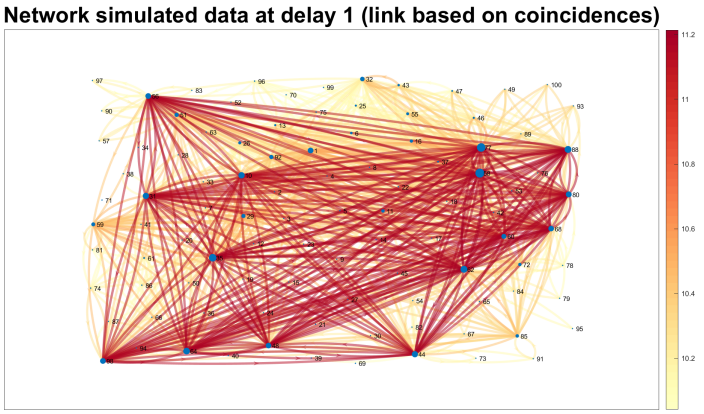

(B)

Figure 32: Neuronal network: (A) The neuronal network with the link based on simulated bursty spike Coincidence at delay 0. (B) The neuronal network with the link based on simulated bursty spike Coincidence at delay 1.

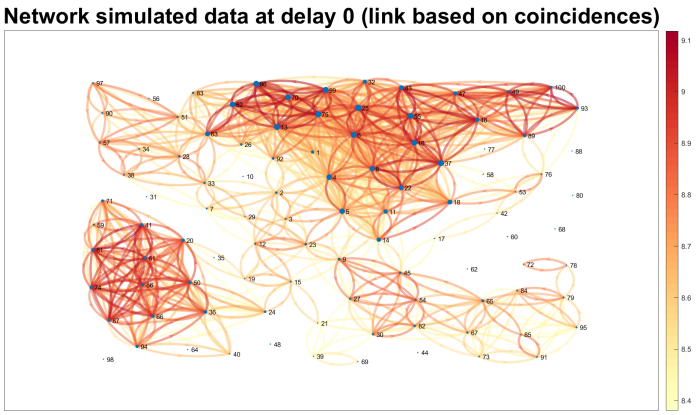

(A)

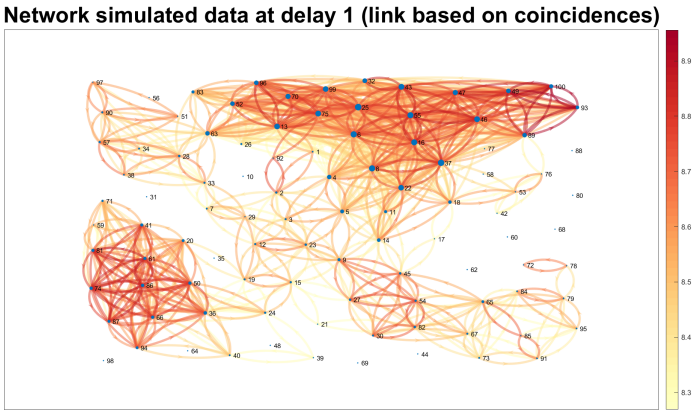

(B)

Figure 33: Neuronal network: (A) The neuronal network with the link based on simulated bursty normalized coincidences at delay 0. (B) The neuronal network with the link based on bursty simulated normalized coincidences at delay 1.

4.2.3 Gaussian filter analysis

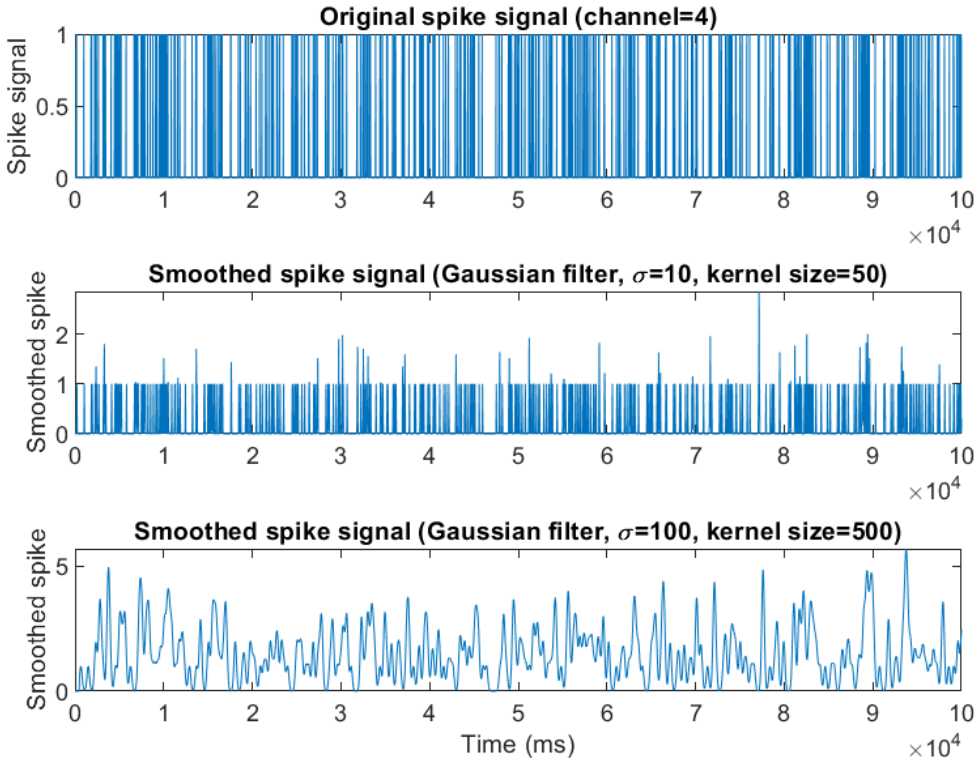

Figure 34: Gaussian filter: The application of a Gaussian filter to the simulated bursty spike data using two different filter standard deviation values: σ = 10 and σ = 100.

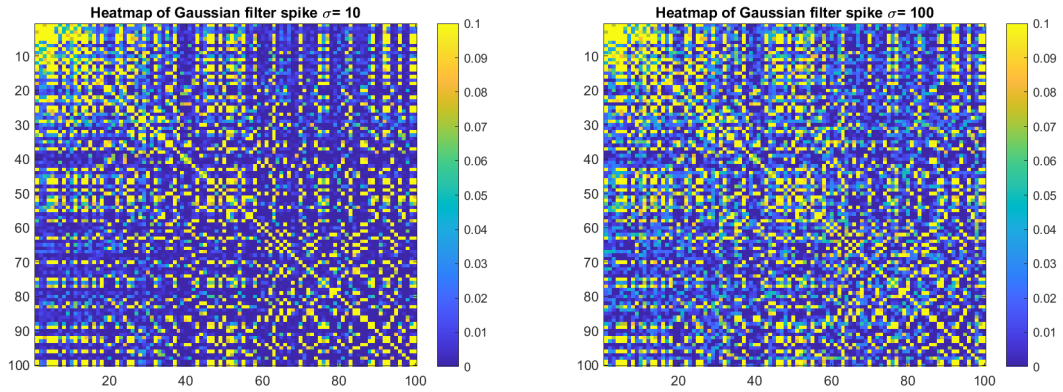

(A) (B)

Figure 35: Coincidences heatmap: (A) The heatmap of Guassian filter for simulated bursty spike at $\sigma = 10$. (B) The heatmap of Guassian filter for simulated bursty spike at $\sigma = 100$.

The last connectivity metric under our consideration is functional connectivity of the filtered time series. Two distinct filter width values were experimented with, namely 10 ms and 100 ms. Figure 34 visually displays the results of implementing the Gaussian filter analysis on a snapshot of a simulated time series. In Figure 35 we show correlation matrices, often referred to as "functional connectivity matrices," derived from the smoothed time series. As in §4.1.3, when the standard deviation of the filter is larger, the correlations generally exhibit higher values.

Figure 36 introduces a scatter plot that illustrates the relationship between ground-truth connectivity and functional connectivity. Notably, a lower standard deviation for the filter amplifies the strength of this association. At a global level, the correlation between GTC and FC stands at R = 0.55 for $\sigma = 10$ and R = 0.53 for $\sigma = 100$. Particularly noteworthy is the substantial influence stemming from EE and EI connections, collectively exerting a positive impact on the observed correlation. For a sigma of 10, these connections yield Pearson correlation coefficients of 0.63 (EE) and 0.67 (EI), while at a sigma of 100, these coefficients translate to 0.62 (EE) and 0.66 (EI) respectively. Additionally, FC values tend to be limited for erroneous II connections. In contrast, IE connections consistently display notable FC values, manifesting a correlation coefficient of R = -0.56 for

$\sigma = 10$ (and R=-0.54 for $\sigma = 100$).

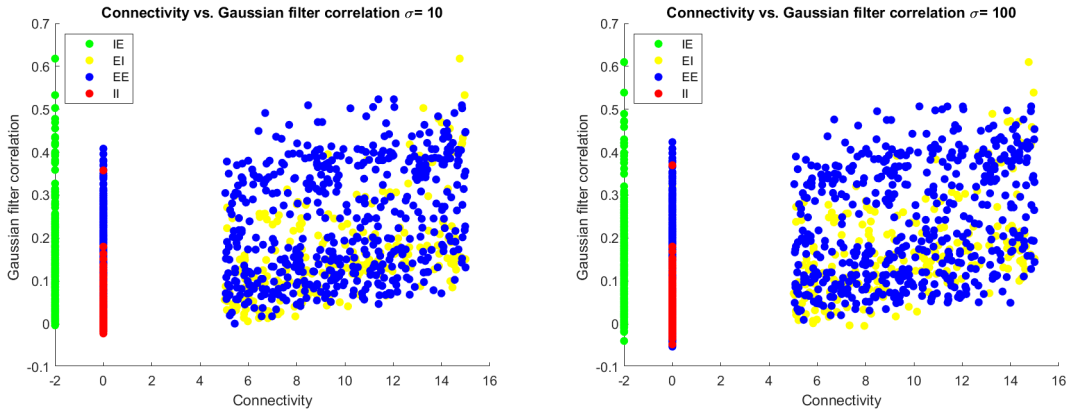

(A) (B)

Figure 36: Connectivity and Gaussian filter correction: (A) Scatter plot between simulated bursty spike time connectivity and Gaussian correction at $\sigma = 10$. (B) Scatter plot between simulated bursty spike time connectivity and coincidences with Significance test at $\sigma = 100$.

4.2.4 Summary

Similar to the analysis of the simulated non-bursty spike scenario, we conducted an assessment of three metrics (transfer entropy, TE; number of spiking coincidences, NSC; Gaussian filter functional connectivity, FC) with the aim of gauging their efficacy in reconstructing the true network connectivity structure.
Compared to the non-bursty scenario, connectivity reconstruction is generally less effective. In particular, it is much more difficult to eliminate spurious coincidences and identify inhibitory connections. The effectiveness of the used metrics greatly hinges on the nature of the specific connection type. TE and FC attribute notable links to certain erroneous II connections. This issue is mitigated to a certain extent by NSC, especially when normalized, particularly at delay 1. EE connections are robustly identified by all methods, with normalized NSC excelling in this regard. IE connections are detectable by all methods, but no method is able to discern the inhibitory characteristic of these connections. In the case of EI connections, all methods identify them, although not as effectively

as they do with EE connections.

Overall, among the tested methods, NSC with a delay emerges as the most effective choice. NSC normalization improves the detection of EE links only.

4.3 Culture data

The data retrieved from cultured neurons which are placed in MEAs (microelectrode arrays) is organized in 100 distinct clusters, each encompassing an arrangement of 3x3 individual neurons. To gain deeper insights from this dataset, a discerning approach was employed whereby the neurons exhibiting the highest levels of activity within each specific cluster were singled out. This selection was predicated on the characteristic firing rates exhibited by these neurons (Figure 37). The spike plot derived from the cultured neuron spiking activity is presented in Figure 38A, together with the accompanying distribution of firing rates across each individual channel. An observation emerges: in the position with our model-simulated datasets with both non bursty and bursty spike patterns, the recorded time series show an intermediate behavior. Some of the recorded neurons exhibit very elevated firing rates (Figure 38B).

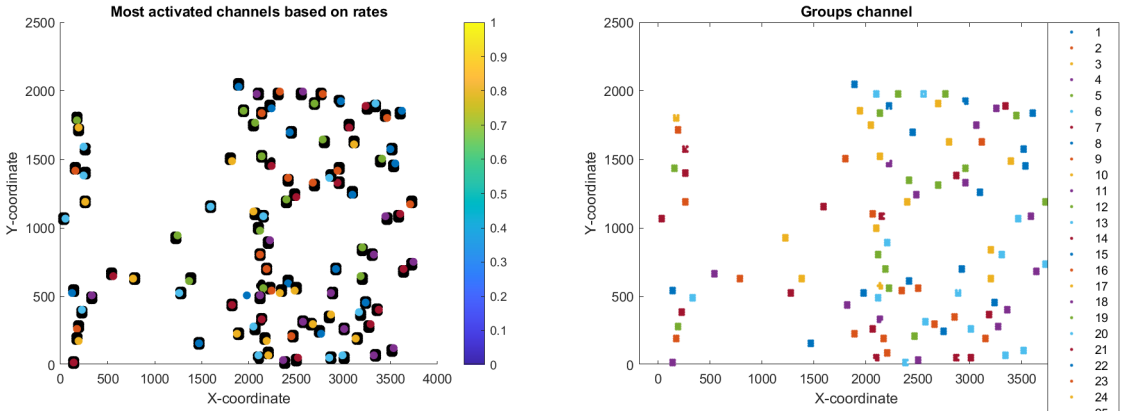

(A) (B)

Figure 37: Neuronal network channel: (A) The neuronal network channel. (B) The neuronal network channel with the highest rates for each channel.

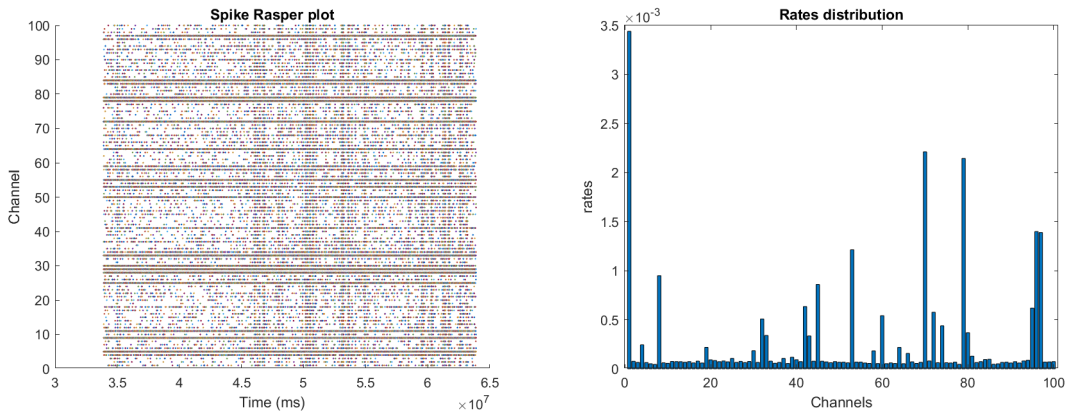

(A) (B)

Figure 38: The neuron raster plot for culture neuron spike: (A) Spiking activity of culture neuron for 100 neurons channel. (B) Channel spike signal applied with Gaussian filter.

4.3.1 TE analysis and null models

In addition to our analysis on simulated spike scenarios, we extended our investigation to encompass culture neurons using both TE and TE with significance assessment. Similarly, we calculate TE values across a range of delays spanning from 1 to 20. From these calculations, we select the maximum TE value associated with each delay. Following this, the unprocessed TE values are subjected to evaluation using a null model (as elaborated upon in §3.4.4), carried out individually for each connection. The outcomes of these analyses are visually illustrated in Figure 39A and 39B, respectively. The distributions for TE and TE with significance test are represented in Figure 40. Before significance testing, a bimodal distribution appears with a large peak corresponding to larger TE strengths and a small peak with weak TE strengths. After testing, the smaller peak disappears. Which indicates the statistical testing process causes the weaker TE strengths to no longer stand out as a distinct peak in the distribution, resulting in a distribution that is more unimodal (single-peaked) with a larger peak corresponding to stronger TE strengths.

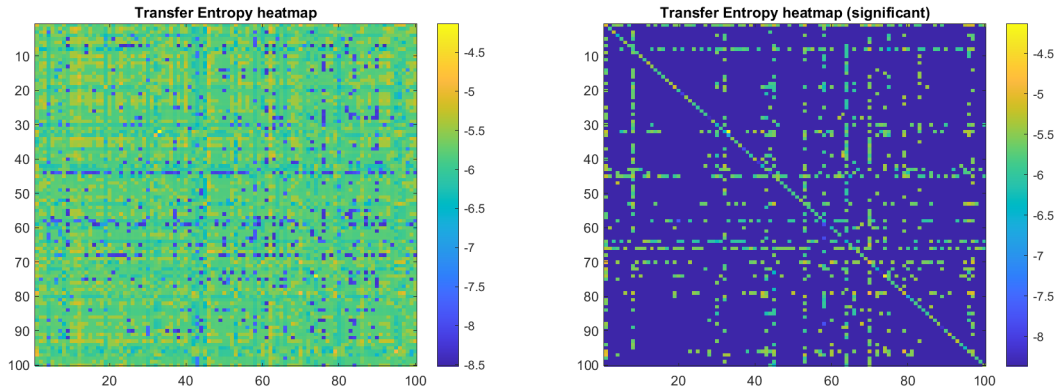

(A) (B)

Figure 39: (A) Heat map of culture neuron TE. (B) Heat map of culture neuron with significance (The significance is computed by iterating 1000 null models by jittering spike times solely from the sender neuron with 5% threshold).

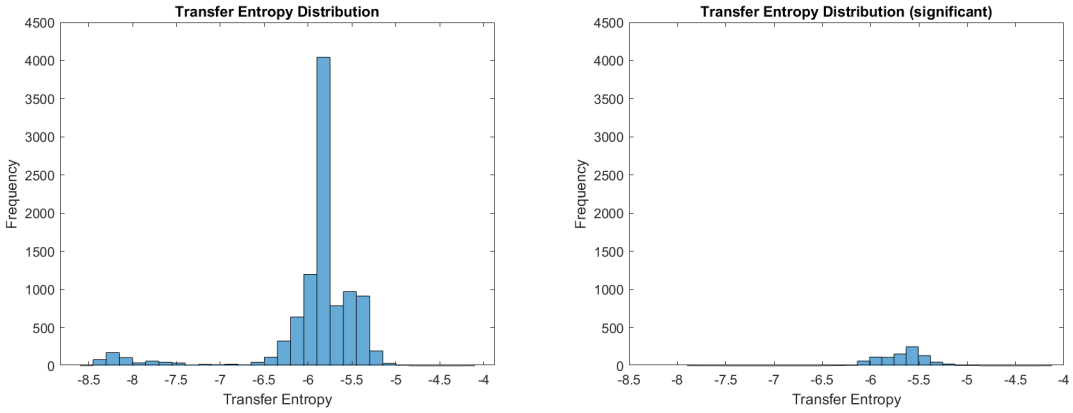

(A) (B)

Figure 40: (A) Distribution of culture neuron TE. (B) Distribution of culture neuron TE with significance (The significance is computed by iterating 1000 null models by jittering spike times solely from the sender neuron with 5% threshold).

The illustration of the neural network's configuration can be found in Figure 41A and 41B, delineating the establishment of connections through both TE and

TE with significance tests. Remarkably, a slight reduction in the number of network connections is evident in the context of TE significance analysis this time compared with our scenario ones. Which indicates that the significance tests are playing a role in filtering out weaker or less meaningful connections, resulting in a more refined network representation.

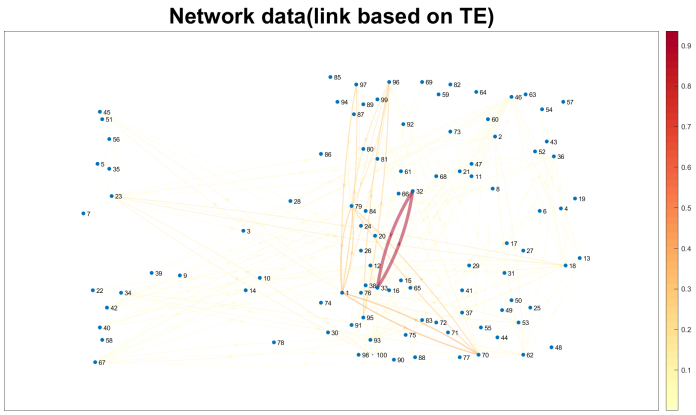

(A)

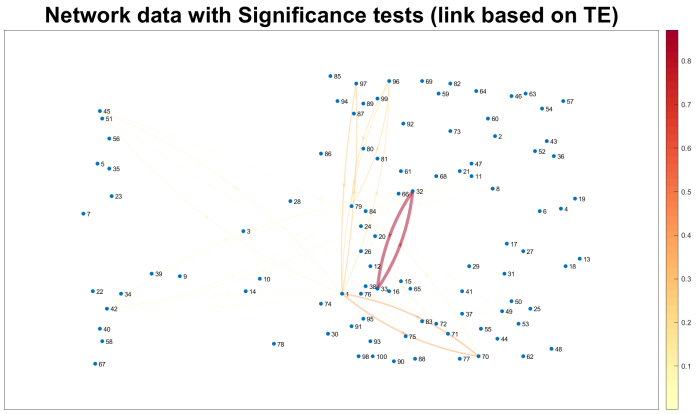

(B)

Figure 41: Neuronal network: (A) The neuronal network with the link based on culture neurons spike TE. (B) The neuronal network with the link based on culture neurons spike TE with significance (The significance is computed by iterating 1000 null models by jittering spike times solely from the sender neuron with 5% threshold).

4.3.2 Coincidences analysis and null models

Our investigation also encompasses an analysis of coincidences within cultured spikes. This exploration is illuminated in Figure 42 through a Heat map that

portrays the coincidences observed across 100 channels in our cultured dataset, considering two distinct temporal delays of 0 and 1. Notably, the graphical representation reveals a notable contrast: at delay 0, a substantial abundance of coincidences is evident, whereas at delay 1, the count of coincidences experiences a significant reduction. Further insight into this phenomenon is provided through the analysis illustrated in Figure 43, which showcases the distribution of coincidences. Specifically, at delay 0, a considerable quantity of coincident events is observed, displaying a decrement towards 100. In contrast, at delay 1, the count of coincident events diminishes, ultimately stabilizing around 5.

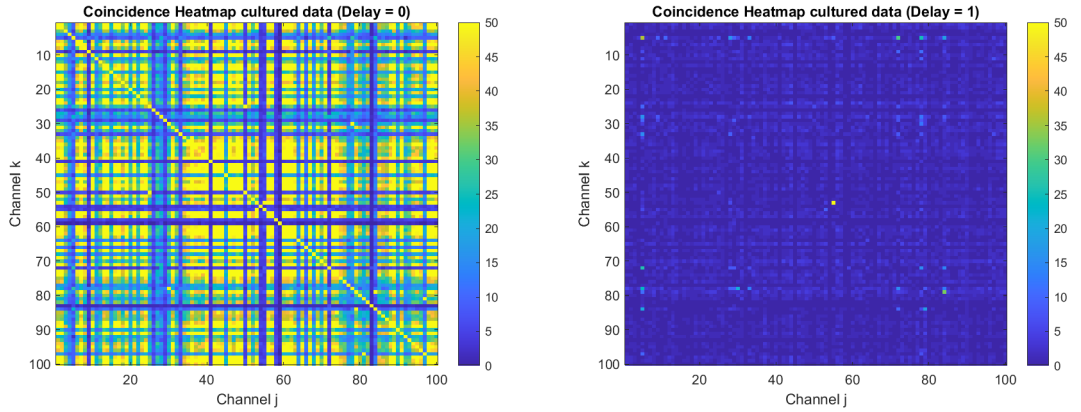

(A) (B)

Figure 42: Coincidences heatmap: (A) The coincidences heat map culture neurons at delay 0. (B) The coincidences heat map of culture neurons at delay 1.

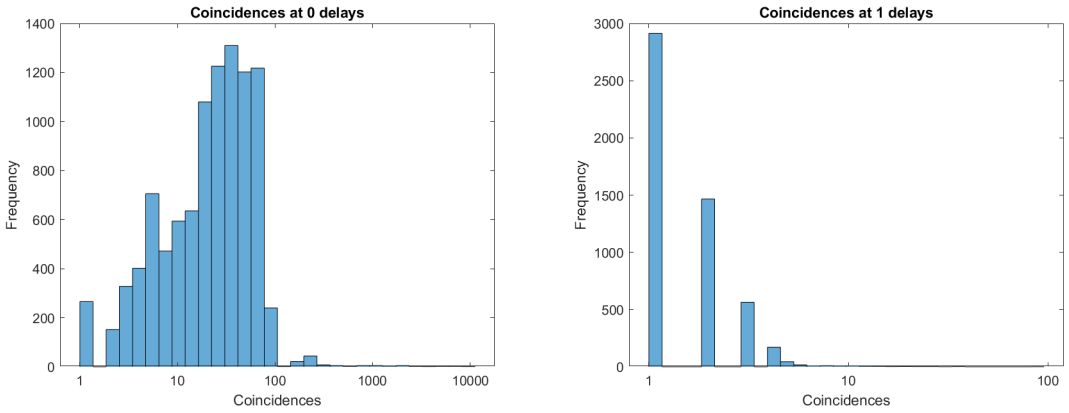

(A) (B)

Figure 43: Distribution of coincidences: (A) The coincidence distribution of culture neurons at delay 0. (B) The coincidence distribution of culture neurons at delay 1.

In the absence of null models in our dataset, the interpretative landscape becomes unfaithful. We can see random noise act as meaningful patterns and lead to the risk of both overestimating and underestimating the significance of observed spike time behaviors. Consequently, our ability to draw accurate conclusions about the underlying neuronal dynamics becomes compromised. By employing null models, we establish a solid statistical foundation for model validation, and the detection of true patterns. This approach ensures that conclusions are backed by solid statistical rationale, enhancing the credibility of findings.
Figure 44A illustrates an occurrence where coincidences with significance testing at delay 0 are primarily driven by neurons with high firing rates. However, in Figure 44B, the dominance of this coincidence pattern diminishes at delay 1. Moving to Figure 45, we provide distributions of coincident events under significance testing for both delay settings. In contrast to the pre-testing distributions, these distributions display a positive skewness.

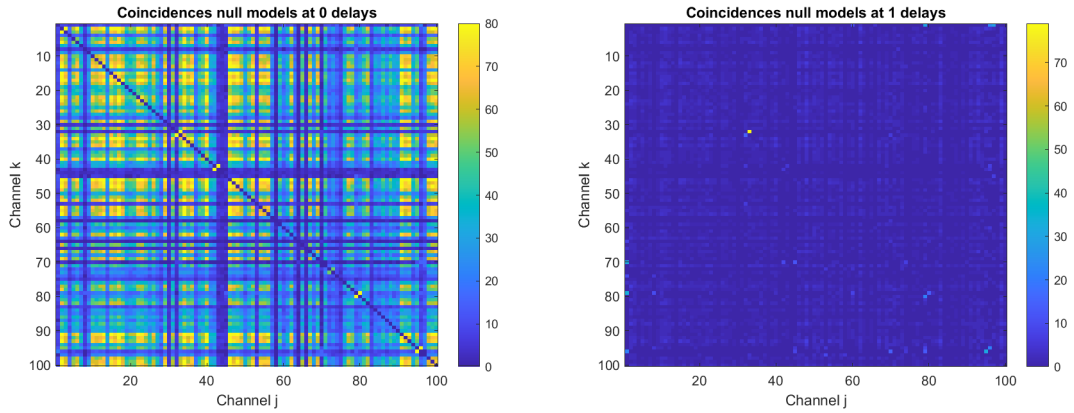

(A) (B)

Figure 44: (A) The coincidences with significance (The significance is computed by iterating 1000 null models by applying random spike times to the data with 5% threshold) heat map of culture neuron spikes for 100 neurons at delay 0. (B) The coincidences with significance (The significance is computed by iterating 1000 null models by applying random spike times to the data with 5% threshold) at delay 1.

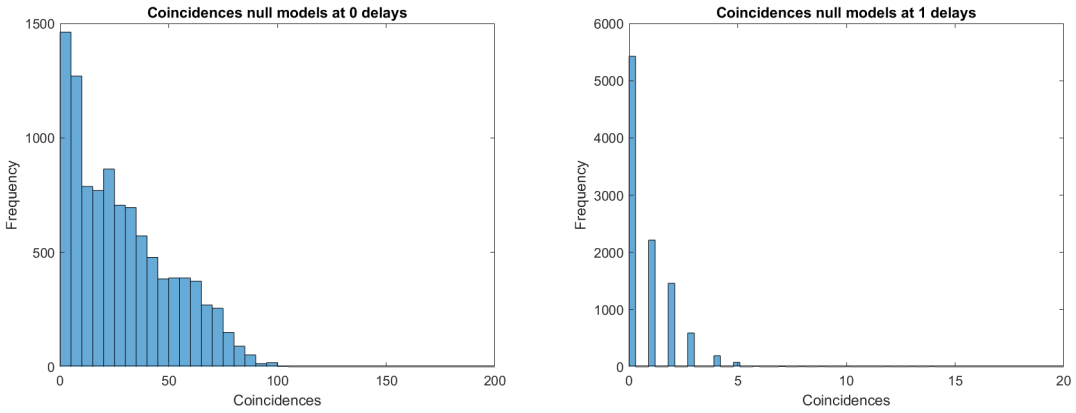

(A) (B)

Figure 45: (A) The coincidences with significance (The significance is computed by iterating 1000 null models by applying random shift to spike times to the data with 5% threshold) distribution of culture neuron spikes for 100 neurons at delay 0. (B) The coincidences with significance (The significance is computed by iterating 1000 null models by applying random spike times to the data with 5% threshold) of culture neuron spikes for 100 neurons at delay 1.

The depiction of the structural arrangement of the neural network is accessible in Figure 46A and 46B. These figures elucidate the establishment of network connections through coincidental events at two distinct temporal offsets, namely 0 and 1. Intriguingly, a noteworthy increment in the strength of network connections becomes apparent when considering coincidental events at delay 1, as compared to the corresponding configuration observed at delay 0. Proceeding to Figure 47, in which we have undertaken the normalization of coincidence values, it becomes evident that, at a delay of 0, the number of coincidences remains consistent when compared to the initially computed coincidences. However, at a delay of 1, there is a significant augmentation in the strength of the connection, as contrasted with the original coincidence data.

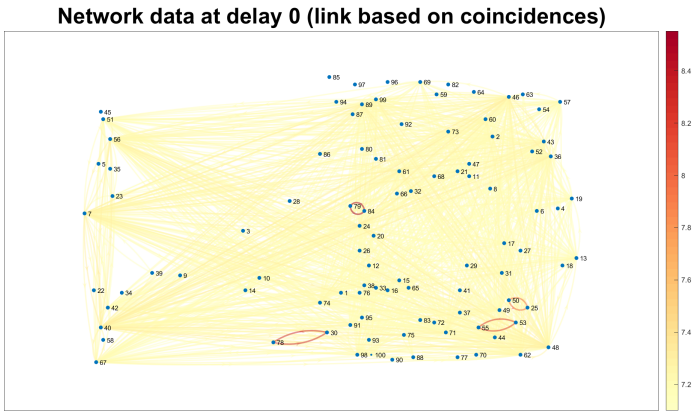

(A)

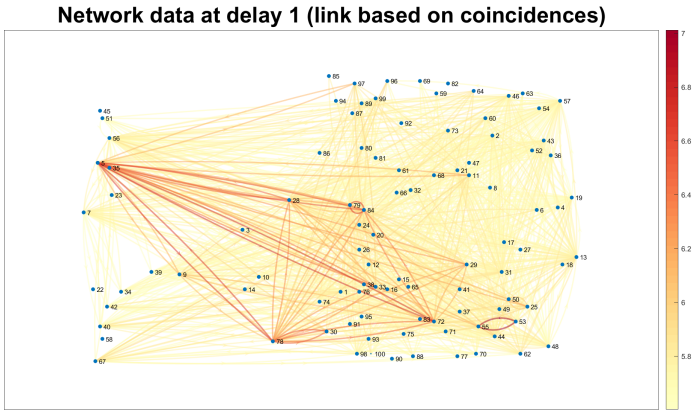

(B)

Figure 46: Neuronal network: (A) The neuronal network with the link based on culture neurons spike Coincidence at delay 0. (B) The neuronal network with the link based on culture neurons spike Coincidence at delay 1.

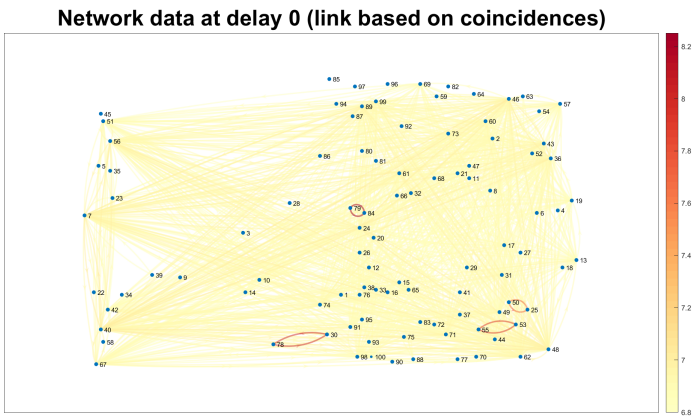

(A)

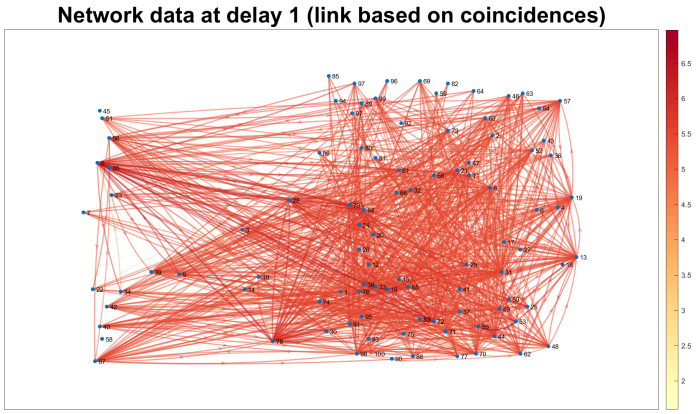

(B)

Figure 47: Neuronal network: (A) The neuronal network with the link based on culture neurons normalized coincidences at delay 0. (B) The neuronal network with the link based on culture neurons normalized coincidences at delay 1.

4.3.3 Gaussian filter analysis

The utilization of Gaussian filter analysis has been extended to our culture dataset, affording a more profound understanding of neuronal plasticity. Our dataset has undergone Gaussian filtering using both sigma 10 and sigma 100 (Figure 48). The outcome is manifest in the discernibly smoothed spike distribution when

employing sigma 100, whereas the effect is comparatively subtle with sigma 10. Complementing this, the generation of a heat map is represented, subsequently depicted in Figure 49 for both sigma 10 and 100. Upon inspection, it becomes evident that sigma 100 reveals a greater prevalence of active data points beyond the diagonal compared to sigma 10.

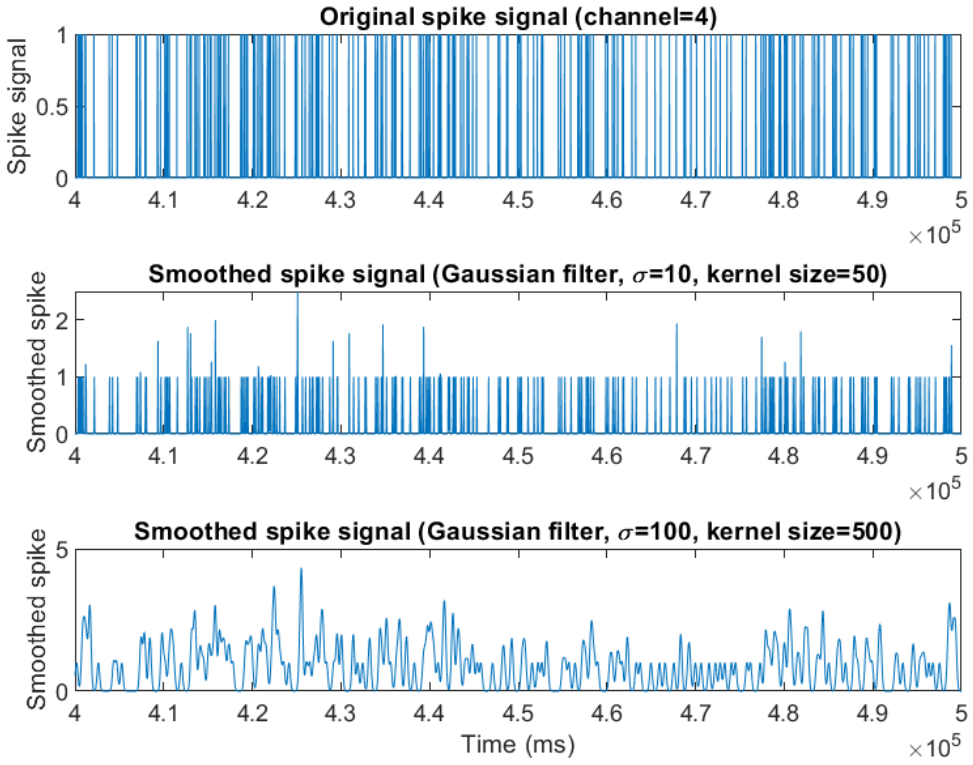

Figure 48: Gaussian filter: The application of a Gaussian filter to the culture neurons spike data using two different filter standard deviation values: σ = 10 and σ = 100.

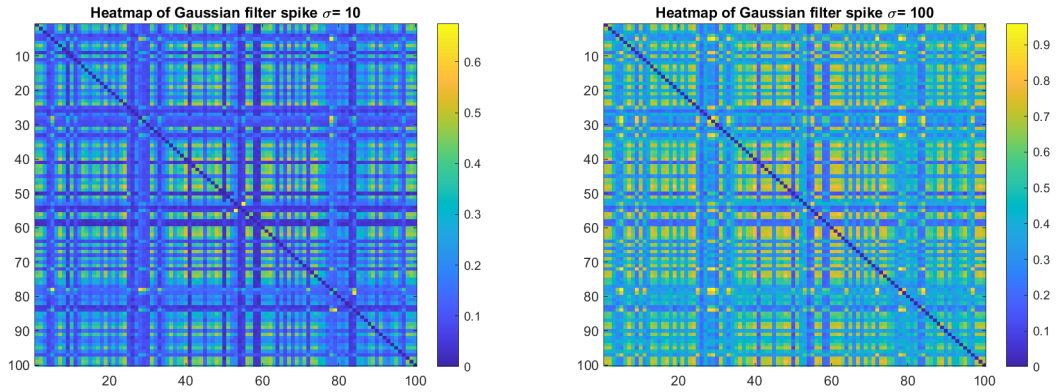

(A) (B)

Figure 49: Coincidences heatmap: (A) The heatmap of Guassian filter for culture neurons spike at $\sigma = 10$. (B) The heatmap of Guassian filter for culture neurons spike at $\sigma = 100$.

4.3.4 Summary

The investigation of culture neurons extended to using TE analysis and null models, together with NSC and its null models. The absence of null models highlighted the challenge of distinguishing meaningful patterns from random noise, impacting the interpretation of spike time behaviors. To address this, the study emphasized the importance of employing null models for accurate conclusions and reliable pattern detection. Null models provided a statistical foundation for model validation, enhancing the credibility of findings. Additionally, Gaussian filter analysis was applied to the culture dataset to understand neuronal plasticity. Gaussian filtering with different sigma values (10 and 100) was performed, resulting in smoothed spike distributions. The effect of sigma 100 was more pronounced, revealing more active data points beyond the diagonal in a generated heat map compared to sigma 10.
Overall, the study utilized various analytical approaches to gain insights from cultured neuron data, emphasizing the significance of null models for accurate interpretation and the application of Gaussian filter analysis to understand neuronal plasticity.

Chapter 5

Discussion

In this study, we aimed to reconstruct the connectivity of a spiking neural network from spike data alone, as obtained through multi-electrode arrays (MEAs). To this aim, we developed and tested three connectivity metrics – Transfer Entropy (TE), Number of Spiking Coincidences (NSC), and Gaussian Filter Functional Connectivity (FC) – in reconstructing the underlying network connectivity structure using simulated data. In our simulations, we featured networks with spatiotemporal activity profiles similar to that of real neuron cultures observed by MEAs. We conducted our analysis in two scenarios: one with non-bursty spike patterns and the other with bursty spike patterns, as biological networks can exhibit one of these two behaviors. Our findings define the effectiveness of these metrics under varying conditions and provide insights into their abilities and limitations.

While all tested metrics were able to reconstruct the ground truth connectivity to a certain extent, their performance was not always comparable. Overall, TE's performance was better than FC's, and NSC's performance was better than TE's offered and increased performance. The reconstruction accuracy heavily depended on the type of connection (inhibitory/excitatory). All methods were relatively effective in measuring excitatory connections, with normalized NSC exhibiting superior performance. Inhibitory connections, though, were nearly always significantly overestimated and exhibited many false positives, especially for TE and FC (normalized NSC effectively mitigated this issue). Furthermore, all methodologies except NSC were not able to explicitly discriminate between the excitatory vs. inhibitory type of connections. Finally, all methods showed

reduced performance in the bursty scenario. Bursty spike patterns introduced additional noise and complexities, leading to a higher rate of false positives and a decreased ability to discern inhibitory connections.

These findings emphasize the importance of accounting for data characteristics when choosing an appropriate metric for network analysis. Tailoring metric selection based on the specific data characteristics and connection types being investigated can significantly enhance the accuracy of network reconstructions. Our findings could guide researchers in choosing appropriate metrics for their specific applications and encourage the development of more robust metrics for bursty data.

While our study provides valuable insights, we acknowledge certain limitations. The results regarding TE (Transfer Entropy) and coincidences obtained from simulated data appear to deviate from those derived from cultural data. Notably, there are instances of spurious events exhibiting exact coincidences, which could potentially be attributed to artifacts introduced by the machine. Therefore, a thorough examination of these exact coincidences is imperative, and their exclusion may be considered. Furthermore, the computational process involved in generating null models for Transfer Entropy (TE) and coincidences proved to be notably time-intensive and resource-demanding. Our simulations might not fully capture the intricacies of real-world neural dynamics. Future studies could explore more complex bursty patterns and further investigate the potential synergies of combining multiple metrics. Additionally, the adaptation of the development of bursty data addressed some of the challenges observed in this study, we need to refine the null models of the bursty data. Moreover, the adjustments made in the development of bursty data patterns have addressed certain challenges identified in this study, which assist us to consider further refinements in the null models for bursty data.

In conclusion, our evaluation of connectivity metrics in both non-bursty and bursty scenarios highlights the nuanced interplay between metric performance and data characteristics. The normalized NSC metric with a delay of 1 emerges as a robust choice, particularly in capturing EE connections and managing the challenges posed by bursty spike patterns. Ultimately, the selection of an appropriate metric should be driven by a deep understanding of the data dynamics and the connection types under investigation.

Chapter 6

Acknowledgement

First and foremost, I wish to express my sincerely appreciation to my supervisor, Dr. Michele Allegra, for the continuous support of my internship and research. His guidance, passion, and extensive teachings have been instrumental in shaping my academic journey. Without his persistent help, the goal of my thesis could not be completed.
I am particularly appreciative of Prof. Stefano Vassanelli, my external thesis supervisor, for providing me the opportunity to be under his supervision and work on his lab.
I extend my heartfelt thanks to Elisa Tentori, a PhD student, for her collaborative spirit, kindness, and unwavering assistance throughout the course of my thesis.
Many thanks to the Department of Physics and Astronomy, where I had a valuable experience in my life.
Last but not least, I would like to thank my beloved Family, who have been always with me and support me unconditionally.

Chapter 7

Bibliography

[1] Hille, B., *Ion channels of excitable membranes.* 2 ed. 1992, Sunderland, MA: Sinauer Associates Inc.

[2] Maschietto, M., Girardi, S., Dal Maschio, M., Scorzeto, M. & Vassanelli, S. Sodium channel β2 *subunit promotes flopodia-like processes and expansion of the dendritic tree in developing rat hippocampal neurons.* Front. Cell. Neurosci. 7, 2 (2013).

[3] Ballini M, Muller J, Livi P, Chen Y, Frey U, Stettler A, Shadmani A, Viswam V, Jones IL, Jackel D, Radivojevic M, et al. IEEE J Solid-State Circuits. 2014; 49:2705. [PubMed: 28502989]

[4] Ballini, M., Müller, J., Livi, P., Chen, Y., Frey, U., Stettler, A., ... & Hierlemann, A. (2014). A 1024-channel CMOS microelectrode array with 26,400 electrodes for recording and stimulation of electrogenic cells in vitro. IEEE journal of solid-state circuits, 49(11), 2705-2719.

[5] Müller J, Ballini M, Livi P, Chen Y, Radivojevic M, Shadmani A, Viswam V, Jones IL, Fiscella M, Diggelmann R, Stettler A, et al. Lab Chip. 2015; 15:2767. [PubMed: 25973786]

[6] E. Hodson, D. Thayer and C. Franklin, "Adaptive Gaussian filtering and local frequency estimates using local curvature analysis," in IEEE Transactions on Acoustics, Speech, and Signal Processing, vol. 29, no. 4, pp. 854-859, August 1981, doi: 10.1109/TASSP.1981.1163641.

[7] Antonello, P. C., Varley, T. F., Beggs, J., Porcionatto, M., Sporns, O., & Faber, J. (2022). Self-organization of in vitro neuronal assemblies drives to complex network topology. Elife, 11, e74921.

[8] Celotto, M., Lemke, S., & Panzeri, S. (2022, July). Estimating the temporal evolution of synaptic weights from dynamic functional connectivity. In International Conference on Brain Informatics (pp. 3-14). Cham: Springer International Publishing.

[9] Friston, K. J. (2011). Functional and effective connectivity: a review. Brain connectivity, 1(1), 13-36.

[10] Grun, S. (2009). Data-driven significance estimation for precise spike correlation. Journal of Neurophysiology, 101(3), 1126-1140.

[11] Ito, S., Hansen, M. E., Heiland, R., Lumsdaine, A., Litke, A. M., & Beggs, J. M. (2011). Extending transfer entropy improves identification of effective connectivity in a spiking cortical network model. PloS one, 6(11), e27431.

[12] Izhikevich, E. M. (2007). Dynamical systems in neuroscience. MIT press.

[13] Izhikevich, Eugene M. "Simple model of spiking neurons." IEEE Transactions on neural networks 14.6 (2003): 1569-1572.

[14] Kandel, E. R., Schwartz, J. H., Jessell, T. M., Siegelbaum, S., Hudspeth, A. J., & Mack, S. (Eds.). (2000). Principles of neural science (Vol. 4, pp. 1227-1246). New York: McGraw-hill.

[15] Ronchi, S., Fiscella, M., Marchetti, C., Viswam, V., Müller, J., Frey, U., & Hierlemann, A. (2019). Single-cell electrical stimulation using CMOS-based high-density microelectrode arrays. Frontiers in neuroscience, 13, 208.

[16] Váša, F., & Mišić, B. (2022). Null models in network neuroscience. Nature Reviews Neuroscience, 23(8), 493-504.